

The ALMaQUEST Survey XII: Dense Molecular Gas as traced by HCN and HCO⁺ in Green Valley Galaxies

LIHWAI LIN,^{1,*} HSI-AN PAN,² SARA L. ELLISON,³ NANASE HARADA,^{4,5} MARÍA J. JIMÉNEZ-DONAIRE,^{6,7} K. DECKER FRENCH,⁸
WILLIAM M. BAKER,^{9,10} BAU-CHING HSIEH,¹ YUSEI KOYAMA,^{11,5} CARLOS LÓPEZ-COBÁ,¹ TOMONARI MICHİYAMA,¹²
KATE ROWLANDS,¹³ SEBASTIÁN F. SÁNCHEZ,¹⁴ AND MALLORY D. THORP¹⁵

¹*Institute of Astronomy & Astrophysics, Academia Sinica, Taipei 10617, Taiwan*

²*Department of Physics, Tamkang University, No.151, Yingzhuang Road, Tamsui District, New Taipei City 251301, Taiwan*

³*Department of Physics & Astronomy, University of Victoria, Finnerty Road, Victoria, British Columbia, V8P 1A1, Canada*

⁴*National Astronomical Observatory of Japan, 2-21-1 Osawa, Mitaka, Tokyo 181-8588, Japan*

⁵*Astronomical Science Program, Graduate Institute for Advanced Studies (SOKENDAI), 2-21-1 Osawa, Mitaka, Tokyo, 181-1855 Japan*

⁶*Observatorio Astronómico Nacional (IGN), C/Alfonso XII, 3, 28014 Madrid, Spain*

⁷*Centro de Desarrollos Tecnológicos, Observatorio de Yebes (IGN), 19141 Yebes, Guadalajara, Spain*

⁸*Department of Astronomy, University of Illinois, 1002 W. Green Street, Urbana, IL 61801, USA*

⁹*Cavendish Laboratory, University of Cambridge, 19 J. J. Thomson Avenue, Cambridge CB3 0HE, United Kingdom*

¹⁰*Kavli Institute for Cosmology, University of Cambridge, Madingley Road, Cambridge, CB3 0HA, UK.*

¹¹*Subaru Telescope, National Astronomical Observatory of Japan, 650 North Aohoku Place, Hilo, HI 96720, USA*

¹²*Faculty of Welfare and Information, Shunan University, 43-4-2 Gakuendai, Shunan, Yamaguchi, 745-8566, Japan*

¹³*Space Telescope Science Institute, 3700 San Martin Dr Baltimore, MD 21218, USA*

¹⁴*Instituto de Astronomía, Universidad Nacional Autónoma de México, Circuito Exterior, Ciudad Universitaria, Ciudad de México 04510, Mexico*

¹⁵*Argelander-Institut für Astronomie, Universität Bonn, Auf dem Hügel 71, 53121 Bonn, Germany*

ABSTRACT

We present ALMA observations of two dense gas tracers, HCN(1-0) and HCO⁺(1-0), for three galaxies in the green valley and two galaxies on the star-forming main sequence with comparable molecular gas fractions as traced by the CO(1-0) emissions, selected from the ALMaQUEST survey. We investigate whether the deficit of molecular gas star formation efficiency (SFE_{mol}) that leads to the low specific star formation rate in these green valley galaxies is due to a lack of dense gas (characterized by the dense gas fraction f_{dense}) or the low star formation efficiency of dense gas (SFE_{dense}). We find that SFE_{mol} as traced by the CO emissions, when considering both star-forming and retired spaxels together, is tightly correlated with SFE_{dense} and depends only weakly on f_{dense} . The specific star formation rate (sSFR) on kpc scales is primarily driven by SFE_{mol} and SFE_{dense}, followed by the dependence on f_{mol} , and is least correlated with f_{dense} or the dense-to-stellar mass ratio (R_{dense}). When compared with other works in the literature, we find that our green valley sample shows lower global SFE_{mol} as well as lower SFE_{dense} while exhibiting similar dense gas fractions when compared to star-forming and starburst galaxies. We conclude that the star formation of the 3 green valley galaxies with a normal abundance of molecular gas is suppressed mainly due to the reduced SFE_{dense} rather than the lack of dense gas.

Keywords: galaxies:evolution – galaxies: low-redshift – galaxies: star formation – galaxies: ISM

1. INTRODUCTION

The link between molecular gas, which is the fuel of star formation, and the rate of forming stars, has been conventionally characterized using the Schmidt-Kennicutt relation (hereafter SK relation; Schmidt 1959; Kennicutt 1998). The SK relation connects the star formation rate (SFR) surface density (Σ_{SFR}) to the molecular gas surface density (Σ_{mol}) as $\Sigma_{\text{SFR}} \propto \Sigma_{\text{mol}}^n$ (or equivalently, $\text{Log } \Sigma_{\text{SFR}} = n \times \text{Log } \Sigma_{\text{mol}} +$

constant). The power index n is found close to unity but varying between 0.7 and 1.4, depending on the galaxy types (late vs. early types; main sequence vs. green valley vs. starburst galaxies; AGN vs. non-AGN hosts, e.g., Colombo et al. 2018; Sánchez et al. 2018; Kennicutt & De Los Reyes 2021; Lin et al. 2022; Baker et al. 2023), physical scales (Lin et al. 2019b; Ellison et al. 2021a; Pessa et al. 2021; Baker et al. 2022), galactic environments (Pessa et al. 2022), large-scale environments (Jiménez-Donaire et al. 2023), local conditions of star formation (star-forming vs. retired regions; Ellison et

* Email: lihwailin@asiaa.sinica.edu.tw

al. 2021b; Lin et al. 2022), and gas tracers (Wong & Blitz 2002; Gao & Solomon 2004; Bigiel et al. 2008).

Among those investigations, the exploration of the molecular gas abundance and its properties at (sub)-kpc scales across different galaxy populations has received significant attention due to the emergence of extensive large optical integral field unit (IFU) surveys and spatial resolution matched observations facilitated by ALMA. Recent studies on kpc scales reveal that the star formation efficiency ($SFE_{\text{mol}} = \Sigma_{\text{SFR}}/\Sigma_{\text{mol}}$) measured on kpc scales depends on global galaxy properties, such as the global specific star formation rate (sSFR; Schrubba et al. 2011; Leroy et al. 2013; Utomo et al. 2018; Colombo et al. 2018; Lin et al. 2019b; Brownson et al. 2020; Sun et al. 2020; Ellison et al. 2021a; Lin et al. 2022; Baker et al. 2023). For example, based on CO(1-0) observations from the ALMA-MaNGA QUEnching and STar formation (ALMaQUEST; Lin et al. 2020) survey, Lin et al. (2022) found that green valley (hereafter GV) galaxies not only show lower molecular gas fractions (f_{mol}), defined as the ratio of the molecular gas surface density to the stellar mass surface density ($\Sigma_{\text{mol}}/\Sigma_{*}$), but also depart from the main sequence (hereafter MS) galaxies in the resolved SK relation (rSK) toward a lower value of Σ_{SFR} at a given Σ_{mol} (also see Lin et al. 2017; Brownson et al. 2020; Ellison et al. 2021a). In other words, green valley galaxies exhibit lower local SFE compared to the galaxies located on the star-forming main sequence, similar to the findings based on global studies (e.g., Saintonge et al. 2017). However, the physical process that controls SFE remains unclear.

While the CO emission lines, in particular the low- J transition such as CO(1-0), are commonly used as the standard tracer of the bulk of molecular gas, the critical density of CO(1-0) emission line is on the order of $\sim 10^3 \text{cm}^{-3}$ and therefore traces not only dense but also diffuse gas that is not necessarily capable of forming stars. On the other hand, HCN and HCO^{+} have a greater critical density ($> 10^4 \text{cm}^{-3}$) and are suggested to better correlate with the star formation rate of galaxies (Gao & Solomon 2004; García-Burillo et al. 2012; Usero et al. 2015; Jiménez-Donaire et al. 2019; Neumann et al. 2023). The molecular gas SFE_{mol} can be written as:

$$\begin{aligned} SFE_{\text{mol}} &= \text{SFR}/M_{\text{mol}} \\ &= \text{SFR}/M_{\text{dense}} \times M_{\text{dense}}/M_{\text{mol}} \\ &= SFE_{\text{dense}} \times f_{\text{dense}}, \end{aligned} \quad (1)$$

where M_{mol} and M_{dense} are the total molecular gas mass and dense molecular gas mass, respectively, SFE_{dense} is the dense gas star formation efficiency, and f_{dense} refers to the dense-to-molecular gas ratio, i.e., the dense gas fraction. Therefore, it leaves two possible explanations for the lower SFE_{mol} of green valley galaxies relative to that of main-sequence galax-

ies. The low SFE_{mol} of green valley galaxies can be attributed to either lower SFE_{dense} or lower f_{dense} than that in main sequence galaxies. Since dense gas is normally more spatially concentrated than both the CO(1-0) and the stellar components (Jiang et al. 2020), using the global HCN/CO ratio does not properly capture the variations in gas phase quantities. Spatially resolved observations are therefore critical for assessing star formation tracers, CO, and HCN (and HCO^{+}) on well-matched scales.

A number of previous works have investigated the role of dense gas in star formation on spatially resolved scales. For example, Longmore et al. (2013) found that SFE_{dense} in Galactic Center of our own Milky Way is significant lower than in the rest of the disk. Detailed studies of individual nearby galaxies revealed that SFE can also depend on the dynamical environments of galaxies (e.g., Querejeta et al. 2019; Sánchez-García et al. 2022). In addition to these case studies, dense gas observations over a statistical sample allow for quantitative characterization of the dependence of SFE_{dense} on various galaxies properties. The EMIR Multiline Probe of the ISM Regulating Galaxy Evolution (EMPIRE; PI: F. Bigiel; Jiménez-Donaire et al. 2019) survey observed 9 nearby disk galaxies with HCN(1-0), HCO^{+} (1-0), and HNC(1-0) lines. The MALATANG (Mapping the dense molecular gas in the strongest star-forming galaxies; Tan et al. 2018; Jiang et al. 2020) survey mapped the HCN(4-3) and HCO^{+} (4-3) line emissions in 23 of the nearest, IR-brightest galaxies with the JCMT telescope. Based on the study of IR-to-HCN measurements of 29 disk galaxies, Usero et al. (2015) found that the inferred SFE_{dense} show a strong dependence on the location in a disk assuming a fixed conversion factor. The ACA Large-sample Mapping Of Nearby galaxies in Dense gas (ALMOND; Neumann et al. 2023) studied the dependence of kpc-scale (2.1 kpc) HCN/CO and SFR/HCN ratios on various structural and dynamical properties of the cloud-scale (150 pc) molecular gas across 25 nearby galaxies. Nevertheless, existing surveys predominantly concentrate on star-forming and IR-bright sources, and spatially resolved dense gas observations for objects with depleted star formation remain scarce. Most recently, French et al. (2023) reported dense gas HCN(1-0), HCO^{+} (1-0), and HNC (1-0) observations for six post-starburst (PSB) galaxies and found that most PSB galaxies have low HCN/CO and HCO^{+} /CO line ratios (< 0.04), suggesting that the low SFR of the PSB population is likely due to the lack of dense gas.

In this work, we obtain ALMA observations for HCN and HCO^{+} emissions as dense tracers with the spatial resolution matched to the existing CO(1-0) observations for 3 GV and 2 MS galaxies selected from the ALMaQUEST survey (Lin et al. 2020). We focus on distinguishing the effects between f_{dense} and SFE_{dense} on driving SFE_{mol} . As the HCN and HCO^{+} emissions are in general fainter than CO by more than

an order of magnitude, we start with the CO-bright sample for both GV and MS targets, allowing us to obtain a possible HCN and HCO⁺ detection within a reasonable amount of ALMA integration time. The sample is thus biased toward galaxies that are not deficient in molecular gas. However, this sample still offers opportunities to investigate the central question we attempt to answer: Is the SFE_{mol} primarily regulated by the fraction of molecular gas in the dense phase (f_{dense}) or SFE_{dense}? Across this paper, the subscript ‘mol’ is adopted to refer to the molecular gas quantities obtained from CO(1-0) observations, whereas the subscript ‘dense’ is used to refer to the dense gas quantities based on HCN(1-0) or HCO⁺(1-0) observations.

In §2, we describe the sample selections and the observational data used in this work. In §3, we present the resolved relation between SFR surface density and dense gas mass surface density (the dense gas version of Schmidt-Kennicutt relation) and investigate the dependence of SFE_{mol} on the SFE_{dense} and the dense-to-molecular ratio (f_{dense}). In §4, we discuss issues affecting the interpretation of this work. Conclusions are given in §5.

Throughout this paper we adopt the following cosmology: $H_0 = 70 \text{ km s}^{-1} \text{ Mpc}^{-1}$, $\Omega_m = 0.3$ and $\Omega_\Lambda = 0.7$. We use a Salpeter initial mass function (IMF).

2. SAMPLE AND OBSERVATIONS

In this work, we study 5 galaxies selected from the ALMaQUEST sample (Lin et al. 2020), which observed 46 galaxies chosen from the Mapping Nearby Galaxies at Apache Point Observatory (MaNGA; Bundy et al. 2015) survey with the Atacama Large Millimeter Array (ALMA) of CO(1-0). Details on the CO(1-0) data reduction and properties are described in the main survey paper (Lin et al. 2020) and the global properties of the molecular gas in ALMaQUEST green valley galaxies are presented in Lin et al. (2022). Table 1 lists the general information of the 5 targets analyzed in this work. Dense gas observations in HCN(1-0) (restframe 88.631 GHz) and HCO⁺(1-0) (restframe 89.189 GHz) of the 5 ALMaQUEST galaxies were carried out with ALMA in Cycle 7 on 2019 using the Band 3 receiver and C43-2 configuration (project code: 2019.1.01178.S; PI: Lihwai Lin). The synthesized beam FWHM is $\sim 2.5''$ that is matched to the MaNGA and CO (1-0) spatial resolutions, which correspond to 1.2-1.5 kpc for the 5 galaxies presented in this work. While the resolution is not sufficient to resolve the giant molecular clouds (GMCs), which is typically several tens of pc, the observations offer investigations at scales that bridge the global to the local properties. For the remainder of the paper, we refer to CO(1-0), HCN(1-0) and HCO⁺(1-0) emissions as CO, HCN and HCO⁺, respectively.

In Figure 1, we display the global properties of the 5 targets (yellow symbols) selected for the dense gas observa-

tions with respect to the remaining 41 ALMaQUEST galaxies (blue symbols). The left panel shows the distribution of galaxies on the integrated (global) specific star formation rate (sSFR) vs. stellar mass (M_*) plane using measurements taken from the Pipe3D (Sánchez et al. 2016a,b) value-added catalog (Sánchez et al. 2018) in the SDSS DR15 release (Aguado et al. 2019). The global f_{mol} vs. SFE_{mol} are displayed in the right panel. We target 3 green valley galaxies with normal f_{mol} but low SFE_{mol} based on the CO measurements. We also observed HCN and HCO⁺ for 2 main sequence galaxies, with predicted HCN and HCO⁺ brightest among those with similar f_{mol} . While f_{mol} of the 3 green valley galaxies is comparable to the 2 main sequence galaxies, their SFE_{mol} is suppressed by a factor of ~ 10 , making their sSFRs among the lowest ones in our sample. This setup allows us to assess the difference in the dense gas abundance relative to the molecular gas, traced by the HCN/CO and HCO⁺/CO ratios, between the main sequence and green valley samples.

Our spectral setup includes one line targeting HCN and three low-resolution spectral windows for checking the continuum. The target-line window has a bandwidth of ~ 930 MHz (3200 km s^{-1}), with a native channel width of $\sim 2 \text{ km s}^{-1}$ and is sufficiently wide to also include the line of HCO⁺. The data were processed by the standard pipeline in the Common Astronomy Software Applications package (CASA version 5.6; McMullin et al. 2007). The systematic flux uncertainty associated with the calibration is typically 5%-10% in Band 3 (see ALMA Proposer’s Guide)

The task tclean was employed for deconvolution with a robust = 0.5 weighting (Briggs). We adopted a user-specified image center, pixel size ($0.5''$), and restoring beamsize ($2.5''$) to match the image grid and the spatial resolution of the MaNGA images. The restoring beamsize is similar to that of the native beamsize reported by the tclean ($2.7'' \times 2.4''$). The HCN and HCO⁺ lines were imaged separately. To increase the signal-to-noise ratio, the spectral channels are binned to 30 to 50 km s^{-1} , varying from galaxy to galaxy. The rms noise of the spectral line data cubes ranges from ~ 0.087 to 0.152 mJy/beam.

The integrated intensity maps of HCN and HCO⁺ were constructed using the task IMMOMENTS in CASA. The integrated intensity maps were created by integrating emission from a velocity range set by hand to match the observed line profile without any clipping in the signal. Figure 2 displays the maps of various emission lines, including CO, HCN, and HCO⁺. As can be seen, the two lines are detected in all our 5 targets. We compute the total intensities of CO, HCN, and HCO⁺ by summing up all the spaxel values within a 1.5 effective radius ($1.5R_e$) provided in the Pipe3D catalog. The total intensity and luminosity of the 5 objects considered in this work are listed in Table 2. The global

Table 1. Global Properties of HCN and HCO⁺ targets

Plate-IFU	Galaxy Type	RA (deg)	DEC (deg)	MaNGA redshift	$\log_{10}(M_*/M_\odot)^{(a)}$	$\log_{10}(\frac{\text{SFR}}{M_\odot \text{yr}^{-1}})^{(b)}$
7815-12705	MS	318.990448	9.543076	0.029550	10.83	0.42
8081-9101	MS	332.798737	11.800733	0.028460	10.60	0.32
8081-12703	GV	331.122894	12.442626	0.025583	10.34	-0.79
8083-6101	GV	332.892853	11.795929	0.026766	10.30	-0.88
8950-12705	GV	42.032784	-0.752316	0.025277	10.53	-0.41

NOTE—^(a) ^(b) Values are taken from value-added catalog (Sánchez et al. 2018) in the SDSS DR15 release (Aguado et al. 2019).

Table 2. Global Properties of HCN and HCO⁺ targets enclosed by 1.5 R_e

Plate-IFU	$\log_{10}(\frac{\text{SFR}}{M_\odot \text{yr}^{-1}})^{(a)}$	$\sigma_{\text{HCN}}^{(b)}$ (Jy beam ⁻¹ km s ⁻¹)	$\sigma_{\text{HCO}^+}^{(c)}$ (Jy beam ⁻¹ km s ⁻¹)	I _{CO} ^(d) (Jy km s ⁻¹)	I _{HCN} ^(e) (Jy km s ⁻¹)	I _{HCO⁺} ^(f) (Jy km s ⁻¹)	$\log_{10}(\text{L}_{\text{CO}}/\text{L}_\odot)^{(g)}$	$\log_{10}(\text{L}_{\text{HCN}}/\text{L}_\odot)^{(h)}$	$\log_{10}(\text{L}_{\text{HCO}^+}/\text{L}_\odot)^{(i)}$
7815-12705	0.47	0.0148	0.0154	32.27729	0.74242	0.85672	8.75	7.34	7.40
8081-9101	0.24	0.0224	0.0174	18.95202	0.54407	0.51363	8.65	7.34	7.31
8081-12703	-1.23	0.0135	0.0167	7.75231	0.23821	0.15411	7.84	6.55	6.36
8083-6101	-1.12	0.0139	0.0112	17.38613	0.55128	0.42021	8.25	6.98	6.86
8950-12705	-1.10	0.0227	0.0201	24.11672	0.30664	0.75681	8.04	6.37	6.76

NOTE—^(a) The total star formation rate converted from H α emissions integrated over 1.5 R_e. ^(b) ^(c) The 1 σ sensitivity of the integrated ALMA intensity maps, calculated using the spectral window shown as the shaded areas in Figure 3. ^(d) ^(e) ^(f) The total line intensity integrated over 1.5 R_e. ^(g) ^(h) ⁽ⁱ⁾ The total line luminosity integrated over 1.5 R_e.

HCN-to-CO and HCO⁺-to-CO flux ratios are measured to be 0.02-0.05 and 0.03-0.05, respectively, broadly consistent with the global values found in previous works (e.g., Usero et al. 2015; Jiménez-Donaire et al. 2019). In Figure 3, we show the ALMA spectra centered on the position of the HCN and HCO⁺ lines using the systematic velocity taken from the NASA Sloan Atlas (NSA) redshift¹, integrated over the region enclosed by 1.5 R_e. The CO spectra from the previous program (Lin et al. 2020) are also overplotted for comparison.

In this work, the molecular gas mass surface density, Σ_{mol} , is computed from the CO luminosity by adopting a constant conversion factor (α_{CO}) of 4.35 M_⊙ (K km s⁻¹ pc²)⁻¹ (e.g., Bolatto et al. 2013), which includes contributions from molecular hydrogen, helium, and heavier elements. Similarly, we convert the HCN and HCO⁺ luminosity into the dense gas mass by adopting the conversion factor $\alpha_{\text{HCN}} = 10 \text{ M}_\odot (\text{K km s}^{-1} \text{ pc}^2)^{-1}$ and $\alpha_{\text{HCO}^+} = 10 \text{ M}_\odot (\text{K km s}^{-1} \text{ pc}^2)^{-1}$ following the suggestions given by Gao & Solomon (2004). While α_{CO} are found to vary from galaxy to galaxy and even within galaxies and various prescriptions have been proposed to predict α_{CO} (e.g., Wolfire et al. 2010; Feldmann et al. 2012; Bolatto et al. 2013; Accurso et al. 2017; Sun et al. 2020; Chiang et al. 2021; Teng et al. 2023), the parameteriza-

tion of the conversion factors of dense gas (α_{HCN} and α_{HCO^+}) at kpc scales, which potentially can depend on the metallicity, remains relatively unexplored. As a result, for the purposes of this study and for making a comparison with other works in the literature, we have chosen to utilize fixed conversion factors. It is noteworthy that the spaxel-based metallicities, computed using the O3N2 diagnostic (Pettini & Pagel 2004; Kewley & Ellison 2008), exhibit median values ranging from 8.69 to 8.76 for each galaxy. The difference is within 0.07 dex of solar metallicity, making a fixed conversion factor for all 5 galaxies a fair assumption.

The MaNGA datacubes utilized in this work are taken from the MaNGA DR15 PIPE3D (Sánchez et al. 2016a,b) value-added products (Sánchez et al. 2018), which contains both global properties of MaNGA galaxies and the spaxel-based measurements of Σ_* and emission-line fluxes. We apply the correction of dust extinction to emission line measurements using the Balmer decrement computed on a spaxel basis assuming an intrinsic H α /H β = 2.86 and a Milky Way extinction curve with R_v = 3.1 (Cardelli et al. 1989). The extinction corrected H α flux is then converted to the SFR following the prescription given by Kennicutt (1998) with a Salpeter IMF. To compute Σ_* and Σ_{SFR} , we normalize the stellar mass and SFR derived for each spaxel to the physical area of one spaxel corrected for inclination taken from NSA. As discussed in Lin et al. (2022), there can be mixed contributions from both the newly formed stars and old stel-

¹ <https://www.sdss4.org/dr17/manga/manga-target-selection/nsa/>

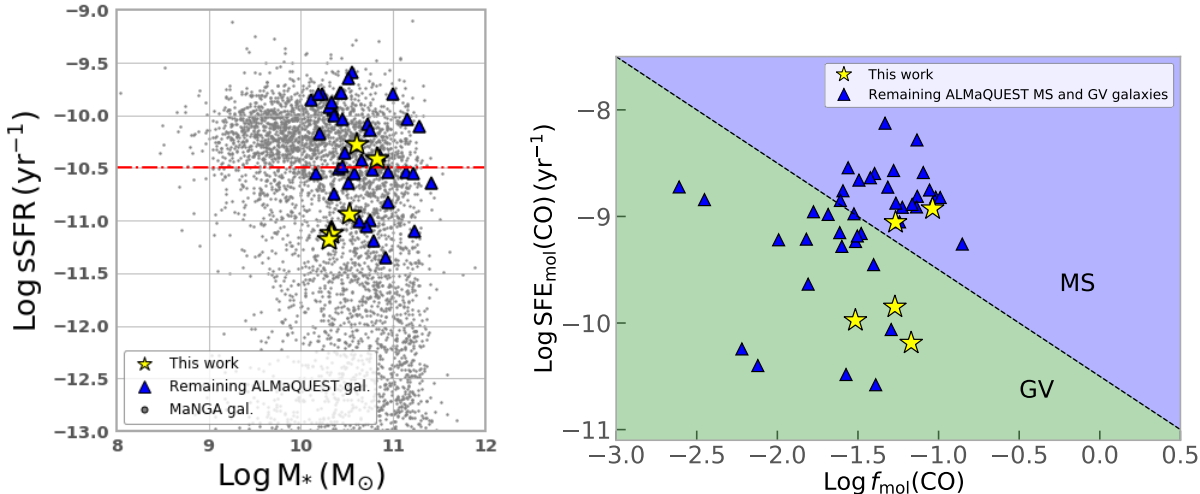


Figure 1. Left panel: The global specific star formation rate (sSFR) vs. stellar mass (M_*) of 4656 MaNGA galaxies (black dots) from the Pipe3D (Sánchez et al. 2016a,b) value-added catalog (Sánchez et al. 2018) in the SDSS DR15 release (Aguado et al. 2019). The yellow star symbols denote the 5 ALMaQUEST galaxies for which we observed in ALMA HCN/HCO⁺ used in this work. The remaining 41 ALMaQUEST galaxies are shown in blue triangles. The red lines denotes the dividing line defining the main sequence (MS) and green valley (GV) subsamples. Our HCN (and HCO⁺) targets are among those with the lowest sSFR rate in the ALMaQUEST green valley sample. Right panel: The molecular gas star formation efficiency (SFE_{mol}) vs. molecular gas fraction (f_{mol}) computed within $1.5 R_e$ using CO for the ALMaQUEST MS and GV subsamples (Lin et al. 2022). The green and blue shaded areas denote the regions that occupy the main sequence and green valley galaxies, respectively, and the color division corresponds to the red dividing line ($\text{Log}_{10}\text{sSFR} = -10.5$) in the left panel. The color symbols are the same as those in the left panel. The three green valley targets with HCN observations have similar CO-based gas fractions but much lower star formation efficiency compared to the main sequence targets.

lar populations to the H α emission, where the former dominant in the star-forming spaxels whereas the latter dominates the retired spaxels (e.g., Stasińska et al. 2008; Singh et al. 2013; Smirnova-Pinchukova et al. 2022). Following Lin et al. (2022), we assume that the H α emission in the star-forming spaxels is purely from active star formation. On the other hand, since the H α emission in the retired regions is mostly powered by evolved stars rather than new star formation, the SFR estimated using the H α to SFR conversion serves only as an upper limit for retired spaxels (Sarzi et al. 2010; Yan & Blanton 2012; Singh et al. 2013; Hsieh et al. 2017; Belfiore et al. 2017; Cano-Díaz et al. 2019; Ellison et al. 2021b).

We limit our analyses to spaxels having signal-to-noise (S/N) > 3 for strong emission lines, i.e., H α and H β lines, $S/N > 2$ for weak lines, such as the [OIII] and [NII] lines, and $S/N > 2.5$ for CO, HCN, and HCO⁺ lines. The choice of the S/N threshold is made by balancing the uncertainty and the number of spaxels. The trends presented in this work are found to be stable against the lower limits of the S/N cut. On the other hand, it is worth noting that the upper limit of the S/N ratio does have an impact on the comparison of the correlation coefficients between different gas tracers when investigating the Schmidt-Kennicutt relations presented in §3.1. We will return to this point in §4.1.

Similar to the methodology we adopted in Lin et al. (2022), we first classify each spaxel into regions where the dominant ionizing source is star formation, composite, or AGN using

the BPT (Baldwin, Phillips, & Terlevich 1981) diagnostic based on the [OIII]/H β vs. [NII]/H α line ratios (Kewley et al. 2001, 2006). We then identify star-forming spaxels to be those satisfying both BPT-classified star-forming criteria and the H α equivalent width (EW) $> 6 \text{ \AA}$ cut (e.g., Cid Fernandes et al. 2011). The retired spaxels are selected to be those having H α $EW < 3 \text{ \AA}$ and $S/N > 3$ in H α (see also Ellison et al. 2021b). The remaining spaxels are categorized as "other" spaxels. These could be either star-forming spaxels but with very low H α EW , composite regions, or non-star-forming regions. As we will see later, the behaviors of these 'other' spaxels are similar to the retired spaxels, indicating that they are predominantly regions with suppressed star formation.

3. RESULTS

3.1. Dense gas Schmidt-Kennicutt Relation

We begin by showing the resolved molecular gas Schmidt-Kennicutt relation, i.e., the star formation rate surface density vs. the molecular gas surface density, for the 2 MS (upper 2 rows) and 3 GV (lower 3 rows) galaxies separately in Figure 4. The gas masses converted based on CO, HCN, and HCO⁺ luminosities are shown from the left to the right panels. Each dot on the plot represents measurements for an individual spaxel. The blue symbols represent spaxels classified as star-forming, the red points denote spaxels classified as retired, and the gray points come from the remaining spaxels. It can be seen that (as expected) the two MS galaxies are

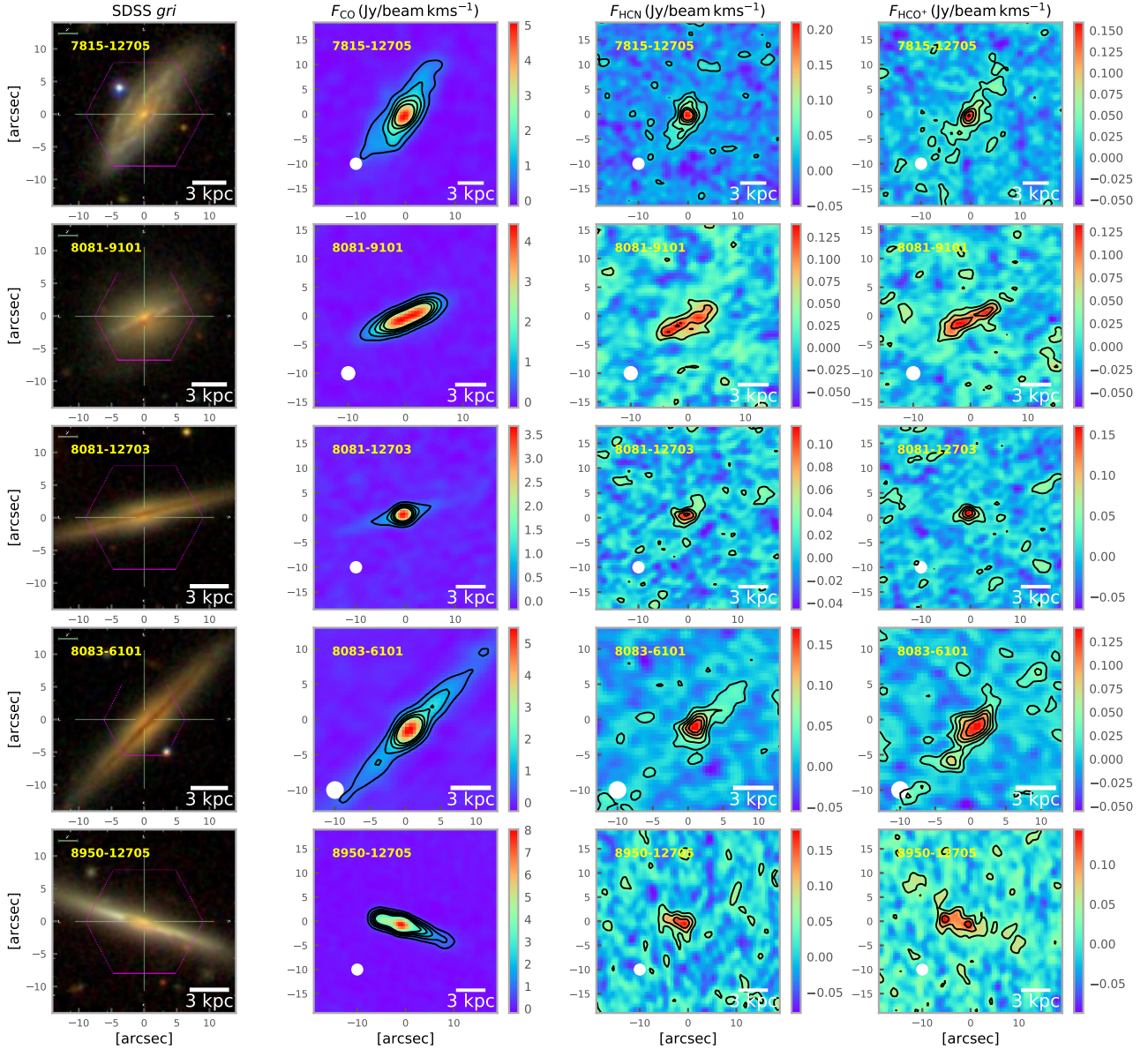


Figure 2. ALMA observations for 5 ALMaQUEST galaxies used in this work. The top two rows are for main sequence galaxies and the bottom 3 rows are for green valley galaxies. From left to right: SDSS *gri* composite images, $^{12}\text{CO}(1-0)$ intensity (Jy km s^{-1} per beam), $\text{HCN}(1-0)$ intensity (Jy km s^{-1} per beam), and $\text{HCO}^+(1-0)$ intensity (Jy km s^{-1} per beam) maps. The back contours denote regions with $S/N = (2,4,6,8,10)$ for HCN and HCO^+ , and regions with $S/N = (10,20,30,40,50)$ for CO observations. The white circle in the lower-left corner of each gas maps illustrates the restoring beamsize. The magenta hexagons denote the MaNGA footprints.

dominated by the star-forming spaxels, whereas the 3 GV galaxies primarily consist of retired and ‘other’ spaxels.

The Pearson correlation coefficients (r) are computed using all types of spaxels and are displayed in each panel. For the main sequence galaxy 7815-12705, Σ_{SFR} is found to correlate with all the three gas tracers (CO, HCN, and HCO^+), although the correlation for HCO^+ is only moderate ($r = 0.5$). Similar behavior is also seen for the other main sequence galaxy 8081-9101. However, in this case the correlation for HCN is weaker compared to either CO or HCO^+ ,

likely affected by the narrow dynamical range in the Σ_{dense} . The correlation coefficients in the CO-based SK relation are in general greater for MS than for GV galaxies. This trend is however less obvious for HCN or HCO^+ -based SK relations.

To guide our eyes when comparing objects-to-objects and spaxel types-to-spaxel types, we fit the star-forming spaxels of the main sequence galaxy 7815-12705 with the orthogonal distance regression (ODR) fitting method for the three gas tracers separately. The best fits of the object 7815-12705 are shown in black as a reference line in the panels of the other

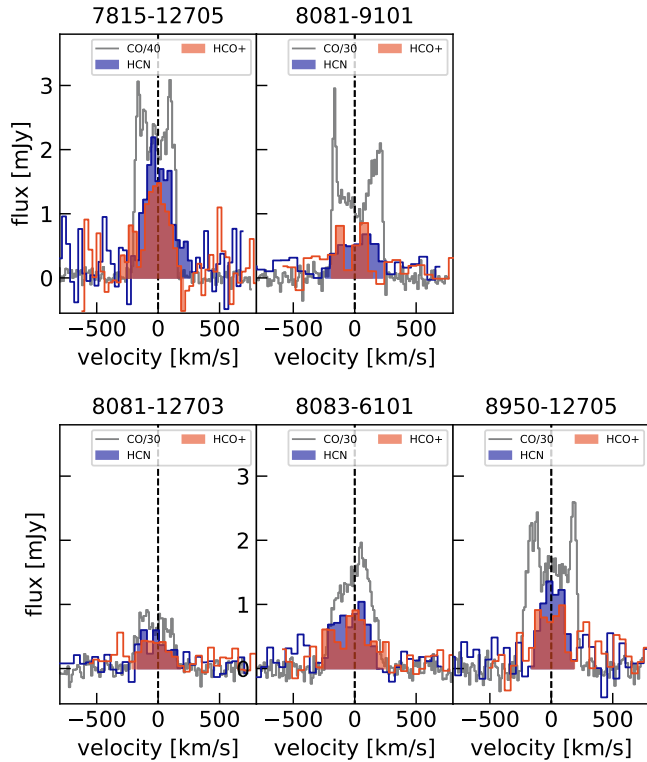


Figure 3. Integrated spectra over the area enclosed by the $1.5 R_c$ with a binned spectral resolution ranging from $30\text{--}50\text{ km s}^{-1}$ for the 5 targets presented in this work. The MaNGA plate-IFU identifier is given above each panel. The blue and red shaded areas represent the region of the spectrum used for computing the HCN and HCO^+ line fluxes, respectively. For comparison, the CO spectra binned at a spectral resolution of 11 km s^{-1} are overplotted and the CO fluxes have been adjusted by applying a scaling factor to fit the figure.

objects as well. The distribution for the retired and other spaxels shows a large scatter and lies toward a lower Σ_{SFR} at a given gas surface density when compared to star-forming spaxels regardless of the gas tracer. It is also apparent that even for the star-forming spaxels, Σ_{SFR} in GV galaxies are systematically lower than those in MS galaxies at a given gas surface density. This is in line with the finding that GV galaxies deviate from the scaling relations formed by MS galaxies not only for retired spaxels but also for star-forming spaxels (Lin et al. 2019b; Brownson et al. 2020; Lin et al. 2022).

Figure 5 is similar to Figure 4 but now we show the spaxel distributions by combining all the 5 galaxies together. In the upper panel, the data points are color-coded by their spaxel types (blue: star-forming; red: retired; others: grey). For comparison, we also plot the EMPIRE sample (magenta points), which consists of 9 galaxies with resolved measurements ($\sim 1\text{--}2\text{ kpc}$ scale resolution) from Jiménez-Donaire et al. (2019). We see that the CO-based SK relation for ALMaQUEST star-forming spaxels is in good agreement with the EMPIRE data points (the upper left panel). On the other

hand, the ALMaQUEST HCN (the upper middle panel) and HCO^+ (the upper left panel) SK relation of the star-forming spaxels are offset from those of the EMPIRE sample toward a lower value of Σ_{SFR} at a given gas mass surface density. It is worth mentioning that the SFR from the EMPIRE sample is based on the total infrared luminosity whereas our sample is converted from the extinction-corrected $\text{H}\alpha$ luminosity. However, the difference in the star formation rate tracers does not seem to be responsible for the systematic difference seen in the dense gas SK relation between our samples since there is a good agreement in the CO-based SK relation. We note that there are in fact significant galaxy-to-galaxy variations even within the EMPIRE sample itself (Jiménez-Donaire et al. 2019) and the ALMaQUEST star-forming spaxels overlap with some of the EMPIRE data points. This suggests that the difference can be intrinsic rather than systematic in the Σ_{SFR} measurements. There are several other speculations that might explain the offset in dense gas SK relation and hence $\text{SFE}_{\text{dense}}$ between EMPIRE star-forming galaxies and the MS targets in this study. These include the potential variations of α_{HCN} and/or α_{HCO^+} (in which case the dense gas conversion factors are overestimated when adopting fixed values), intrinsic differences in $\text{SFE}_{\text{dense}}$ within the star-forming main sequence galaxies, and calibration issues. Given that much less is known about the dense gas conversion factors in any kind of extragalactic system, we cannot be certain that the fixed conversion factors hold for the galaxies in this study or even for EMPIRE. Nevertheless, in the case the SK relation of our MS sample is not representative, unlike EMPIRE galaxies, the offset in $\text{SFE}_{\text{dense}}$ at a given Σ_{dense} between typical star-forming galaxies (as inferred by EMPIRE) and the green valley galaxies is even larger than what we conclude in this work.

Within the ALMaQUEST sample, it is clear that the star-forming and retired spaxels occupy distinct parameter spaces with each other. The non-star-forming (retired plus other) regions do not follow the same scaling relation as the star-forming spaxels and possess lower SFE. While this feature is already known when adopting the CO tracer from earlier works (e.g., Lin et al. 2022), the fact that the same trend also exhibits for the dense gas tracers is not fully expected. The deviation from the dense gas Schmidt-Kennicutt relation basically suggests that the level of star formation activities is not entirely regulated by the amount of available dense gas. Other physical conditions also play roles in determining whether the dense gas is able to form stars or not. Several earlier studies (Gao & Solomon 2004; Wu et al. 2005; Lada et al. 2010) proposed a linear correlation between HCN and SFR, indicating a fixed value of $\text{SFE}_{\text{dense}}$, spanning scales from clouds to galaxies. However, more recent investigations have revealed significant variations in the $\text{SFE}_{\text{dense}}$, across diverse galactic environments and cloud properties (e.g., Longmore

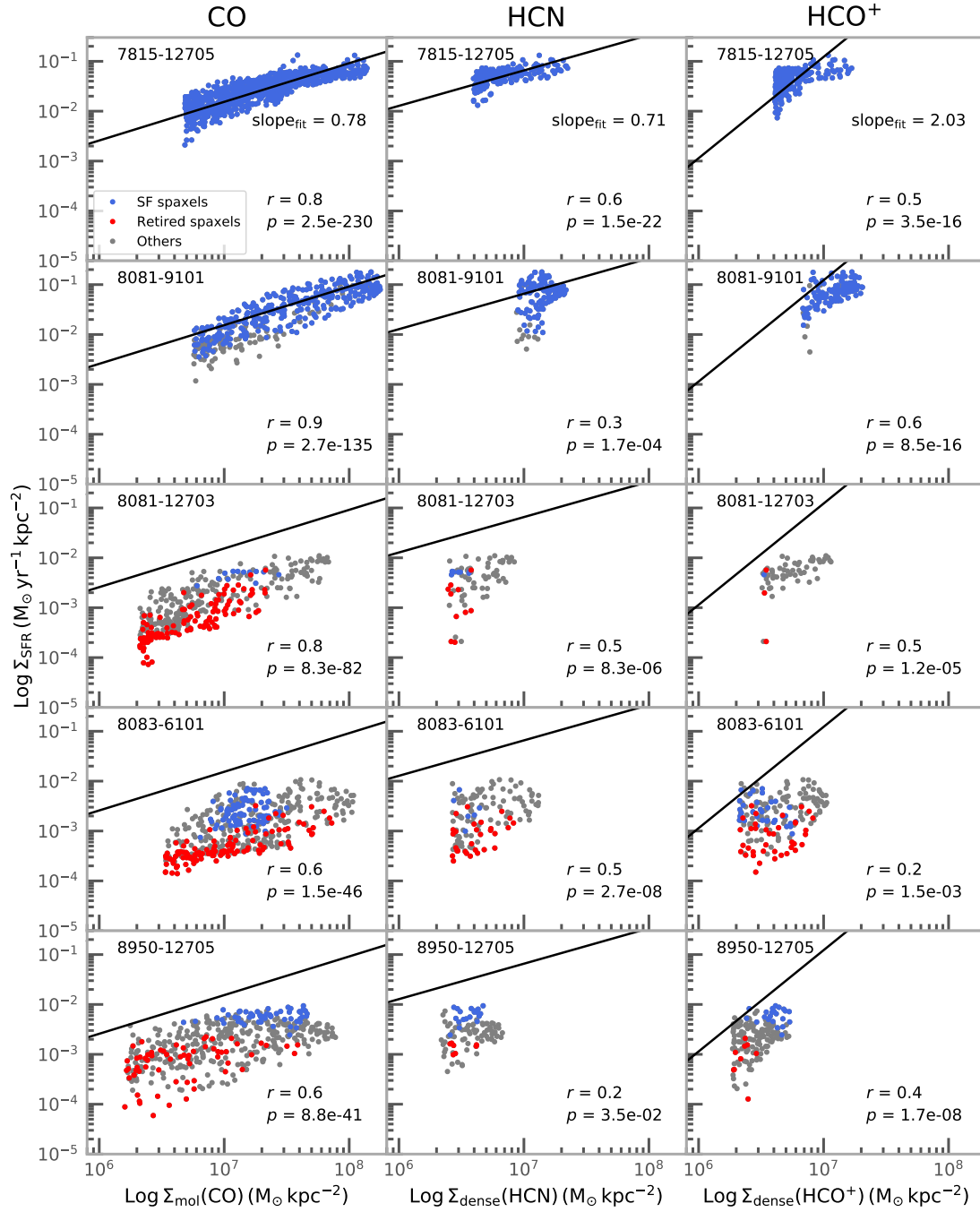


Figure 4. The resolved Schmidt-Kennicutt relation (i.e., SFR surface density vs. gas mass surface density) using various gas tracers. From left to right: CO, HCN, and HCO⁺. The top two rows are for main sequence galaxies and the bottom 3 rows are for green valley galaxies. Each data point represents the measurement from individual spaxels. The sharp edges of the data points in the low end of gas mass surface density correspond to the 2.5- σ detection limits. The star-forming spaxels, retired spaxels, and the remaining spaxels are shown by blue, red, and grey symbols, respectively. At a given gas tracer, the black line represents the best fit of the star-forming spaxels of the MS galaxy 7815-12705 and is the same for all other panels corresponding to a particular gas tracer to guide the eyes. The values of the Pearson (r) correlation coefficients and p -values computed using all spaxels are reported in each panel.

et al. 2013; Usero et al. 2015; Jiménez-Donaire et al. 2019; Querejeta et al. 2019; Sánchez-García et al. 2022; Neumann et al. 2023). Our findings align with this notion, demonstrating that SFE_{dense} is not a constant and varies with the spaxel type.

In the bottom panels of Figure 5, we color code the spaxels by the types of their host galaxies (blue: MS; green: GV). As expected, MG and GV occupy distinct parameter spaces in this diagram since MS galaxies are dominated by star-forming spaxels whilst GV galaxies comprise primarily the non-star-forming spaxels. Therefore, we conclude that the 3 GV galaxies have distinct SFE_{mol} and SFE_{dense} from the 2 MS galaxies despite that they have similar f_{mol} by selection.

3.2. Is the molecular gas SFE dependent on the dense gas fraction?

Equation 1 suggests that the overall molecular gas star formation efficiency (SFE_{mol}) could depend on two things, the dense-to-molecular gas ratio (f_{dense}) and the dense gas star formation efficiency (SFE_{dense}). We now first investigate whether SFE_{mol} is primarily driven by f_{dense} or not. If the answer is ‘yes’, we should expect a positive correlation between SFE_{mol} and f_{dense} .

The upper panels of Figure 6 shows SFE_{mol} against f_{dense} , computed using the HCN (left panel) and HCO^+ (right panel). There is a weak correlation between the x- and y-axes for the star-forming spaxels, indicating that SFE_{mol} is mildly connected to the dense gas fraction in star-forming regions. Turning next to the non-star-forming regions, we see that these spaxels have lower SFE_{mol} than the star-forming spaxels as expected based on the work of Lin et al. (2022). However, it is notable that, despite their very different SFE_{mol} , the two types of spaxels (star-forming vs. non-star-forming) share a similar range of f_{dense} . This implies that the low SFE_{mol} that leads to quenching in non-star forming regions is not due to the lack of dense gas.

In the bottom panels of Figure 6, spaxels are color-coded based on the types of galaxies they belong to: the main sequence (MS; blue points) and green valley (GV; green points) galaxies. We also plot the histograms of f_{dense} for the two types of galaxies. As mentioned earlier, the majority of spaxels in MS galaxies correspond to star-forming regions, while those in GV galaxies are predominantly non-star-forming spaxels. As a result, it is evident from the plot that while the spaxels in MS and GV galaxies exhibit distinct distributions in terms of SFE_{mol} , they demonstrate similar distributions of f_{dense} , emphasizing that f_{dense} does not play a significant role in determining the difference in SFE_{mol} between MS and GV galaxies. This phenomenon is similar to what have been found in some gas-rich early-type galaxies (Crocker et al. 2012) and a certain fraction of post-starburst

galaxies (French et al. 2023). We will return to this issue in §4.2.

3.3. Is the molecular gas SFE dependent on the dense gas SFE?

In the previous sub-section, we found that there was only a weak correlation between SFE_{mol} and f_{dense} . We, therefore, suggested that a similar range of dense gas fractions between star-forming and non-star-forming spaxels supports differences in dense gas star formation efficiency as the primary quenching mechanism. In this sub-section, we test this hypothesis directly.

In the upper two panels of Figure 7, we show the molecular gas-based SFE as a function of the dense gas-based SFE (left: HCN; right: HCO^+). It is obvious that there is a strong dependence of SFE_{mol} on SFE_{dense} , as indicated by the high correlation coefficients (0.93-0.95) even when all types of spaxels are considered together regardless of whether they are star-forming spaxels or not. The ODR best fits for star-forming spaxels are shown in blue lines as a reference. Interestingly, it can be seen that the non-star-forming spaxels also follow a similar trend to the one that is formed by the star-forming spaxels, unlike the bimodal distribution on the SFE_{mol} and f_{dense} plane between the star-forming and non-star-forming spaxels as seen in Figure 6.

In the bottom panels of Figure 7, we present similar plots but this time we color code the spaxels according to their host galaxies: blue for main sequence galaxies and green for green valley galaxies. It can be seen that the GV spaxels extend the distribution of MS spaxels towards lower values of SFE_{mol} and SFE_{dense} . This again reflects the fact that GVs in our sample are dominated by non-star-forming spaxels in contrast to main sequence galaxies, which consist primarily star-forming spaxels.

One caveat of the correlation analysis when discussing the relative importance between f_{dense} and SFE_{dense} in determining SFE_{mol} is that SFE_{mol} and f_{dense} share the same denominator (i.e., Σ_{mol}) while SFE_{dense} and SFE_{mol} share the same nominator (i.e., Σ_{SFR}), which can lead to artificial correlations in both cases. To test this effect, we generate synthesized datasets by shuffling Σ_{mol} and Σ_{dense} and repeat the correlation analysis in §3.2 on the SFE_{mol} vs. f_{dense} relation. The procedure is then repeated 500 times. The median Pearson correlation coefficient r from 500 trials is increased to $r = 0.36$ and $r = 0.34$ using the synthesized data for HCN and HCO^+ , respectively, which is slightly greater than the correlation of the real datasets ($r = 0.1 - 0.3$). We can therefore robustly conclude that there is no apparent dependence on f_{dense} .

Similarly, we test this effect on the SFE_{mol} and SFE_{dense} relation by shuffling both Σ_{mol} and Σ_{SFR} . This time, the median correlation coefficients from 500 trials are already found to

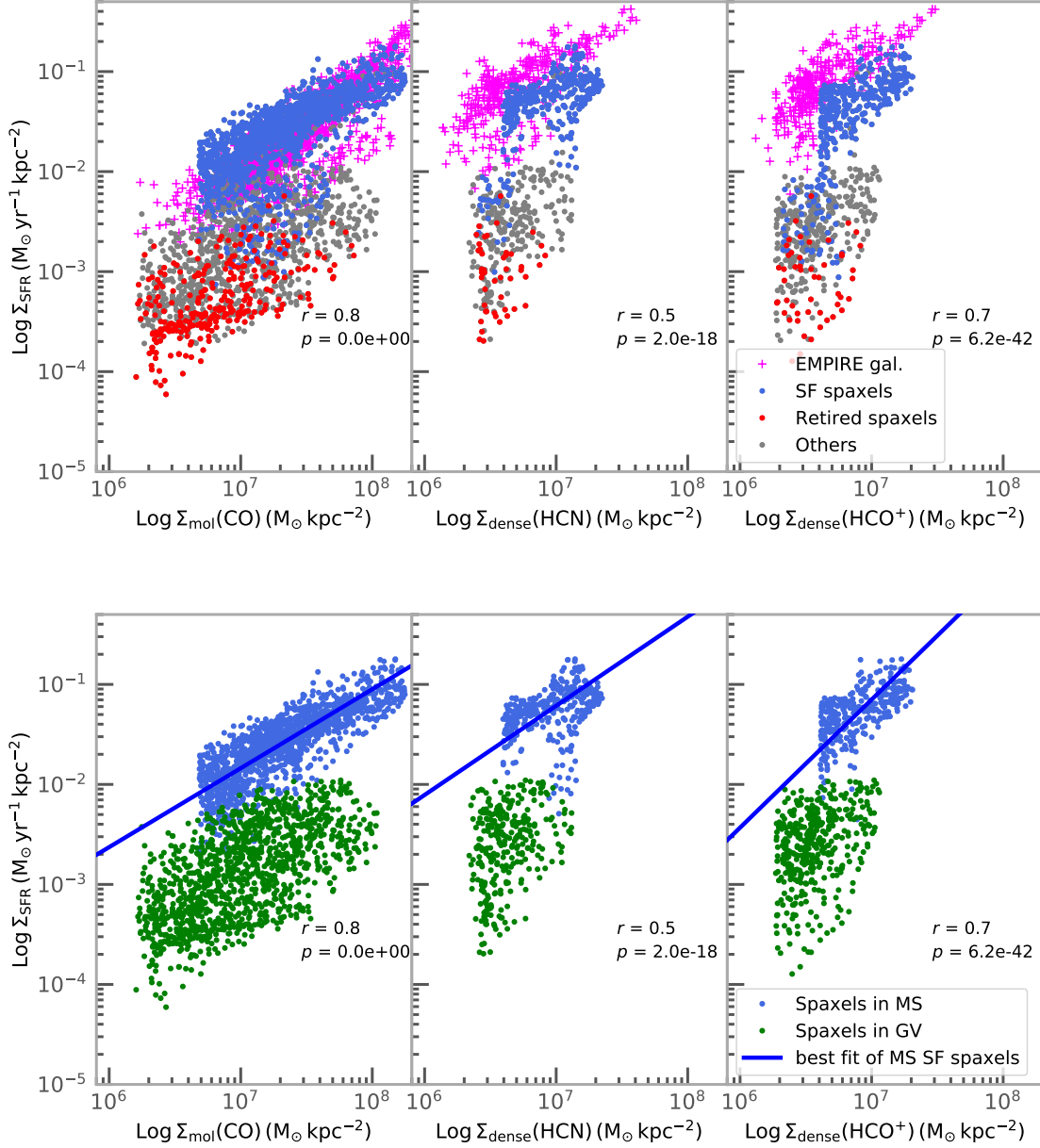


Figure 5. The resolved Schmidt-Kennicutt relation (i.e., SFR surface density vs. gas mass surface density) using various gas tracers, with all galaxies plotted together. The sharp edges of the data points in the low end of gas mass surface density correspond to the $2.5\text{-}\sigma$ detection limits. From left to right: CO, HCN, and HCO^+ . The magenta line represents the best fit from the EMPIRE sample (Jiménez-Donaire et al. 2019) for comparison. Upper panels: The star-forming spaxels, retired spaxels, and the remaining spaxels are shown by blue, red, and grey symbols, respectively. Bottom panels: The spaxels located in the main sequence (MS) and green valley galaxies (GV) are shown by blue and green symbols, respectively. The scatters of the star-forming spaxels relative to the fit are labeled in the lower right corner of each panel. In all panels, the Pearson correlation coefficients (r) and p -values are computed using star-forming spaxels belonging to MS galaxies only.

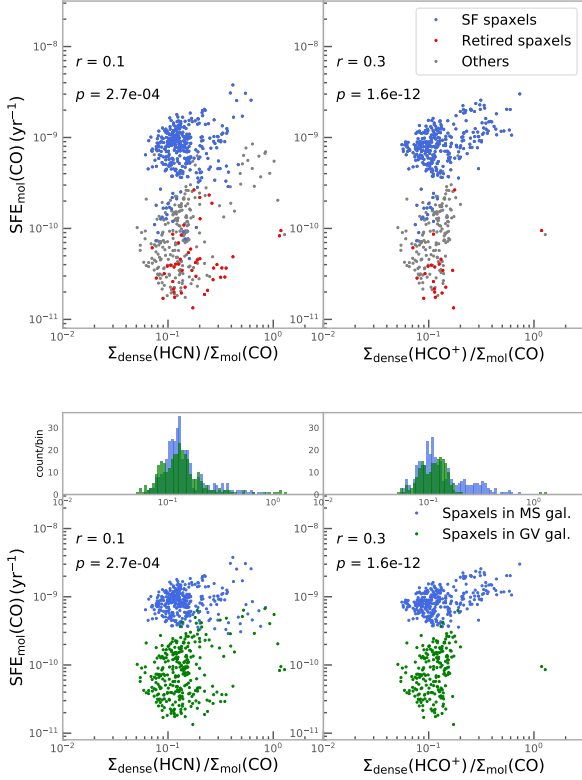


Figure 6. The molecular gas-based SFE_{mol} against the dense-to-molecular mass ratio using HCN (left panel) and the dense-to-molecular mass ratio using HCO^+ (right panel). The Pearson correlation coefficients (r) and p -values computed using all spaxels are reported in each panel. Top panels: the star-forming, retired, and remaining spaxels are shown in blue, red, and grey colors, respectively. Bottom panels: spaxels in MS and GV galaxies are shown in blue and green colors, respectively. Histograms of f_{dense} for both MS and GV galaxies are presented in the upper x-axes.

be high, ~ 0.87 and 0.85 for the case of HCN and HCO^+ , respectively, only slightly lower than the correlations when using the real physical dataset ($r = 0.93$ for HCN and 0.95 for HCO^+), making it difficult to interpret the results. As the artificial correlation arises due to the stretch of the common nominator (Σ_{SFR} in this case), they are sensitive to the dynamical range in Σ_{SFR} . We therefore conduct another experiment, by only selecting data points in the central half of the Σ_{SFR} range, specifically $-3 < \text{Log}_{10}\Sigma_{SFR} < -1.5$, to mitigate this effect. In this case, the correlations for the real datasets are 0.85 (HCN) and 0.84 (HCO^+) and those for the synthesized datasets are 0.70 (HCN) and 0.65 (HCO^+). The difference becomes more apparent in this subset of sample. While it remains difficult to quantify the intrinsic correlations, the central point is that the correlation between SFE_{mol} and SFE_{dense} is stronger when using the real physical dataset than in the synthesized data, in contrast to the worse correlation between SFE_{mol} vs. f_{dense} in the real datasets than

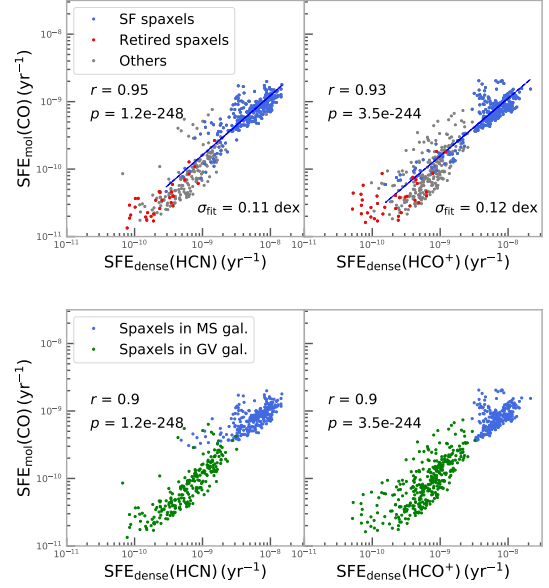


Figure 7. The molecular gas-based star formation efficiency (SFE_{mol}) against the dense gas-based star formation efficiency (SFE_{dense}) that are measured using HCN (left panel) and HCO^+ (right panel). The Pearson correlation coefficients (r) and p -values computed using all spaxels are reported in each panel. Top panels: The star-forming, retired, and remaining spaxels are shown in blue, red, and grey colors, respectively. The blue line represents the best fit of the star-forming spaxels from all 5 objects. The scatters of the star-forming spaxels relative to the fit are labeled in the lower right corner of each panel. Bottom panels: spaxels in the main sequence and green valley galaxies are color-coded by blue and green, respectively.

that in the synthesized data. This hints that the dependence of SFE_{mol} on SFE_{dense} has more physical connection than on f_{dense} in a relative sense. Therefore, the low SFE_{dense} is more likely the primary driver of the low SFE_{mol} in GV galaxies.

3.4. $sSFR$ vs SFE with different tracers

Having discussed the relative importance between f_{gas} and SFE_{dense} in determining SFE_{mol} , we now turn to one of the central questions of this work, which is to identify the major mechanism that is responsible for lowering the specific star formation rate in galaxies. Recalling that $sSFR$ is the product of SFE and f_{gas} , i.e., $sSFR = f_{gas} \times SFE$, in which f_{gas} and SFE could be either expressed using the overall molecular gas or dense molecular gas. It is possible to differentiate the contributions between the gas abundance and star formation efficiency by investigating the dependence of $sSFR$ on f_{gas} and SFE . Here we express the $sSFR$ as the following:

$$\begin{aligned}
 sSFR &= \Sigma_{SFR} / \Sigma_* \\
 &= \Sigma_{SFR} / \Sigma_{dense} \times \Sigma_{dense} / \Sigma_* \\
 &= SFE_{dense} \times R_{dense},
 \end{aligned} \tag{2}$$

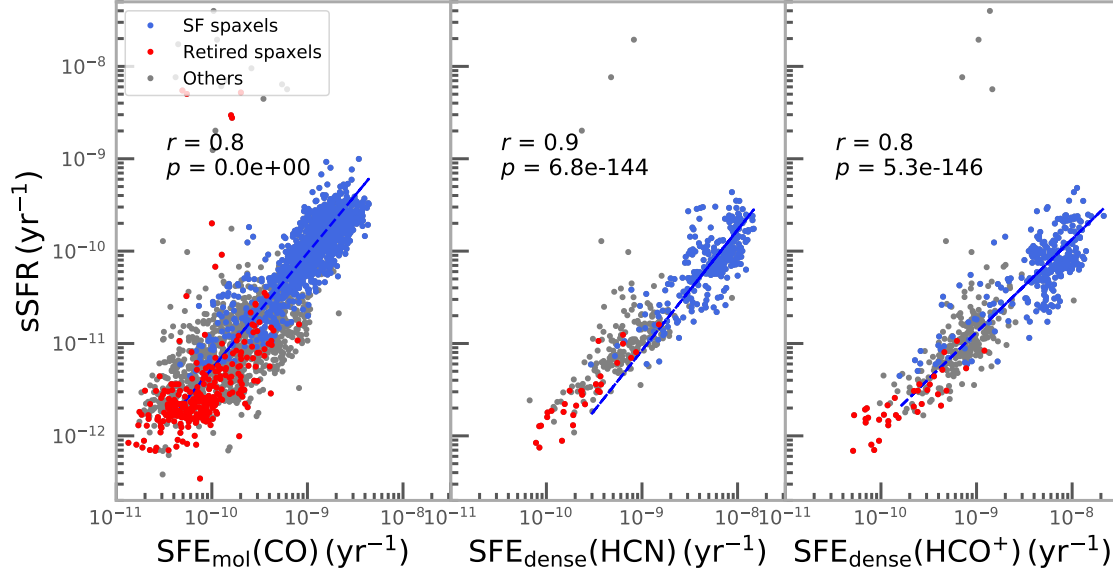


Figure 8. The specific star formation rate against the molecular gas-based SFE measured using CO (left panel), dense gas-based SFE measured using HCN (middle panel), and dense gas-based SFE measured using HCO^+ (right panel). The star-forming, retired, and remaining spaxels are shown in blue, red, and grey colors, respectively. The blue line represents the best fit of the star-forming spaxels from all objects. The Pearson correlation coefficients (r) and p -values computed using all spaxels are reported in each panel.

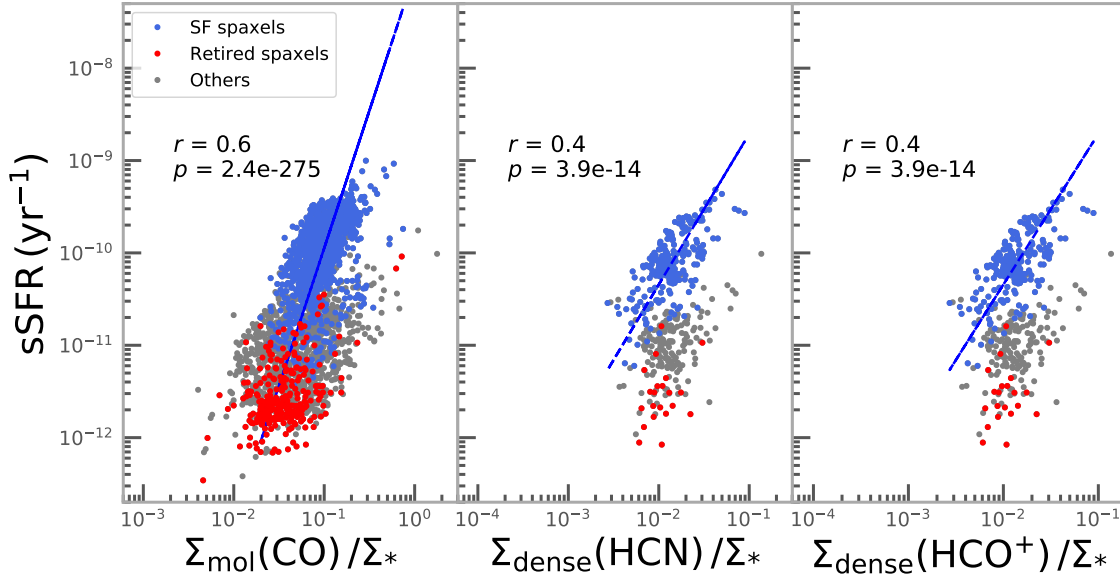


Figure 9. The specific star formation rate (sSFR) against the molecular gas-to-stellar mass ratio (left panel), dense gas-to-stellar mass ratio using HCN (middle panel), and dense gas-to-stellar mass ratio using HCO^+ (right panel). The star-forming, retired, and remaining spaxels are shown in blue, red, and grey colors, respectively. The blue line represents the best fit of the star-forming spaxels from all objects. The Pearson correlation coefficients (r) and p -values computed using all spaxels are reported in each panel.

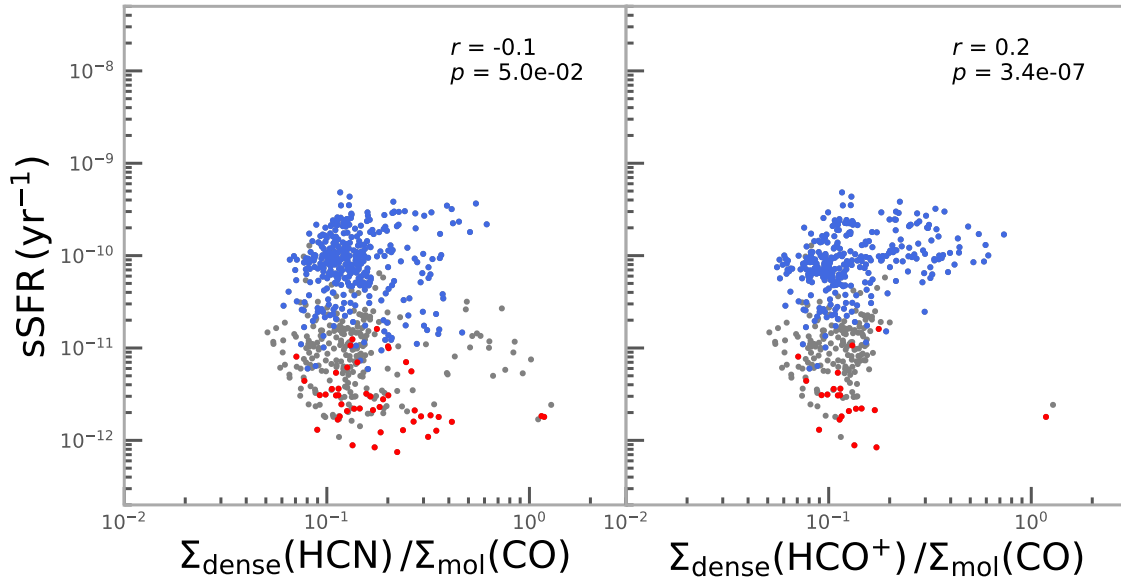


Figure 10. The specific star formation rate (sSFR) against the dense-to-molecular gas mass ratio measured using HCN (left panel) and HCO⁺ (right panel). The star-forming, retired, and remaining spaxels are shown in blue, red, and grey colors, respectively. The Pearson correlation coefficients (r) and p -values computed using all spaxels are reported in each panel.

where R_{dense} is the ratio of the dense gas mass to the stellar mass. This should not be confused with the dense gas fraction (f_{dense}) defined previously, which refers to the dense gas to the molecular gas mass ratio.

We first look at the dependence of sSFR on SFE using various tracers, including CO(1-0), HCN, and HCO⁺. Again in the well-accepted scenario that the stars are formed within the dense molecular clouds, we shall expect a tighter link between sSFR and HCN- or HCO⁺- based SFE than that between sSFR and CO-based SFE. Figure 8 plots the relations of sSFR against the SFE defined with various tracers (CO, HCN, and HCO⁺). We see that in every case there is a strong correlation between sSFR and SFE, regardless of the tracers being used. The correlation coefficients are comparable between the CO-based SFE and the HCN- (or HCO⁺-based) SFE. Another interesting feature is that the non-star-forming spaxels also follow the same trend as the one formed by the star-forming spaxels, suggesting that SFE plays a key role in determining sSFR across the whole range of star formation levels from active to quiescent phases.

On the other hand, the correlation between sSFR and the gas-to-stellar mass ratio is much weaker (see Figure 9) compared to the relation between sSFR and SFE reported in Figure 8. When we consider all types of spaxels together (including star-forming and non-star-forming spaxels), the correlation is only apparent in the case of CO, in which the non-star-forming spaxels also lie on the trend formed by the star-forming spaxels. On the other hand, in the case of HCN or HCO⁺, the non-star-forming spaxels show a departure from the sSFR vs. gas-to-stellar mass ratio that is formed by the star-forming spaxels. In addition, the non-star-forming spaxels share a similar range in the dense gas-to-stellar mass ratio as the star-forming spaxels. Our results suggest that while the dense gas-to-stellar mass ratio does play a role in regulating the sSFR for star-forming spaxels, it is not a dominant factor in determining the sSFR in regions that are undergoing quenching processes.

Equation 2 can also be further expanded as the following:

$$\begin{aligned} sSFR &= SFR/M_{\text{dense}} \times M_{\text{dense}}/M_{\text{mol}} \times M_{\text{mol}}/M_{*} \\ &= SFE_{\text{dense}} \times f_{\text{dense}} \times f_{\text{mol}}. \end{aligned} \quad (3)$$

Therefore, we also investigate the relation between sSFR and f_{dense} , which is shown in Figure 10. It can be seen that there is no apparent dependence of sSFR against f_{dense} in either the case of HCN or HCO⁺. In summary, among several parameters we have explored, the dependence of sSFR on SFE_{dense} (and/or SFE_{mol}) is stronger than on f_{dense} or f_{mol} , suggesting the star formation efficiency is the dominant factor determining the kpc-scale sSFR.

4. DISCUSSION

4.1. Scatter in Schmidt-Kennicutt relations

The critical densities for HCN and HCO⁺ (up to $n_{\text{crit}} \sim 10^{5-6} \text{ cm}^{-3}$) to be excited are much higher compared to that of CO ($n_{\text{crit}} \sim 10^3 \text{ cm}^{-3}$), and therefore they are expected to trace the dense gas that is more relevant to star formation. In this regard, it is natural to expect a tighter correlation in the dense gas-based SK relation than in the CO-based SK relation, as illustrated by early works (e.g., Gao & Solomon 2004; Wu et al. 2005; Lada et al. 2010). This trend, however, is not obvious in our data, in which we show that the correlations between SFR and gas surface density, when limited to the star-forming spaxels, are in fact comparable with each other when using different molecular gas tracers (see Figure 5). This might imply that for the two main sequence galaxies considered here, either HCN or HCO⁺ actually traces gas with density lower than their critical densities (Harada et al. 2019; Evans et al. 2020), for example, through the radiative trapping effects or because of the contributions of high masses of the low-density gas (Shirley 2015; Leroy et al. 2017; Jiménez-Donaire et al. 2019), or they are excited through other mechanisms, such as electron excitation (Goldsmith & Kauffmann 2017), UV from the young massive stars, X-ray from AGNs, and cosmic rays from supernova explosions (Papadopoulos et al. 2014; Topal et al. 2016), which influence the molecular line ratios in different ways (Meijerink et al. 2007; Topal et al. 2016).

Before seeking the physical explanations, we first consider whether our results are impacted by the lower signal-to-noise ratios (S/N) of HCN and HCO⁺ lines when compared to that of CO. This discrepancy in S/N ratios may potentially lead to weaker correlations in the dense gas SK relation compared to the CO-based SK relation. To examine this effect, we repeat the correlation analyses for the star-forming spaxels in main sequence galaxies but impose an upper limit of S/N(CO) = 10 this time. The Pearson correlation coefficient of the CO-based SK relation is found to reduce from 0.8 to 0.6, becoming comparable to the values for HCN (0.5) and HCO⁺(0.7). This test suggests that whether or not the CO-based SK relation is superior to the dense gas SK relation is highly sensitive to the S/N ratios achieved by a given molecular line.

In addition to the effect from the S/N ratio, we note that the dynamical range in the dense gas surface density in our sample is rather narrow and the number of data points is small, compared to other studies (e.g., EMPIRE shown as magenta in Figure 5). These might also impact the measurements of intrinsic of correlations.

Next, we consider the possibility where HCN or HCO⁺ are excited through processes other than collisional excitation. In this case, the HCN/HCO⁺ ratio can vary depending on which mechanism plays a dominant role. Numerical models predict that the flux ratio of HCN/HCO⁺ can be greater than unity in photon dissociation regions whereas HCN/HCO⁺ < 1 in

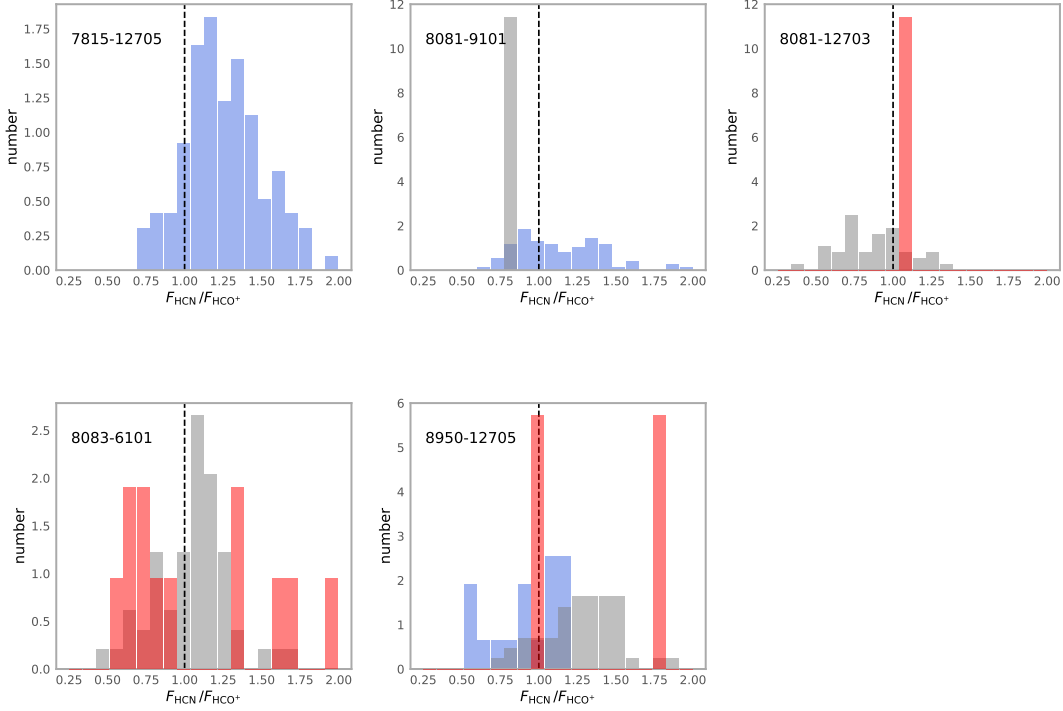


Figure 11. The HCN-to-HCO⁺ flux ratio of the 5 galaxies analyzed in this work. The star-forming, retired, and the remaining spaxels are shown in blue, red, and grey colors, respectively. The vertical dashed line represents the HCN-to-HCO⁺ flux ratio = 1 to guide the eyes.

X-ray dissociation regions if the density exceeds 10^5 cm^{-3} and if the column density is larger than 10^{23} cm^{-2} (Meijerink et al. 2007; Topal et al. 2016). On the other hand, XDR HCN/HCO⁺ ratio becomes larger than one if the column density is less than $10^{22.5} \text{ cm}^{-2}$ (Meijerink et al. 2007). While it is not possible to robustly constrain column densities with current datasets, it is nevertheless insightful to look at the HCN/HCO⁺ ratio in our sample.

Figure 11 shows the histograms of the HCN/HCO⁺ ratio for the 5 galaxies individually. One can see that 4 out of 5 galaxies have HCN/HCO⁺ > 1 in most spaxels. The BPT diagnostics show no signs of AGN spaxels in these 4 galaxies, suggesting that the physical condition of the interstellar medium (ISM) is consistent with photodissociation regions (PDRs). On the other hand, galaxy 8081-12703, one of the GV galaxies, has the spaxel distributions centered at HCN/HCO⁺ ratio ~ 1 , systematically lower than the values of other galaxies. About half the spaxels have the HCN/HCO⁺ ratio less than 1, indicating that this galaxy might be affected by either AGN or supernova explosions. The BPT diagnostics using the [OIII] 5007/H β vs. [NII] 6584/H α ([OIII] 5007/H β vs. [NII] 6584/H α) ratios reveal that the central spaxels are consistent with composite (star-

forming + LINER regions) and may indicate the presence of central AGN. Nevertheless, this galaxy only has very few star-forming spaxels (Figure 4) that contribute to the dense gas SK relation of star-forming spaxels (Figure 5).

Based on the above tests and evidences, we therefore conclude that the ‘tighter’ relation in the CO-based SK relation compared to the dense gas SK relation we see in Figure 5 is more likely driven by the difference in the S/N ratios and also impacted by the small number statistics rather than a genuine behavior. While the lower S/N ratios of the dense gas tracers compared to CO result in a small dynamical range of Σ_{dense} that impacts the fits of the SK relation, our finding that the spaxels in the green valley (GV) exhibit lower $\text{SFE}_{\text{dense}}$ compared to those in the star-forming main sequence (MS) remains valid. This difference is nearly an order of magnitude at a given Σ_{dense} , significantly larger than the uncertainties (less than 40%) associated with the S/N ratio cuts.

Finally, we note that the wide range of $\text{SFE}_{\text{dense}}$ found in this work, spanning two orders of magnitude, seems to be in contrast to the constant $\text{SFE}_{\text{dense}}$ model, in which $\text{SFE}_{\text{dense}}$ is approximately constant once the gas surface density is above a certain threshold (Lada et al. 2012; Evans et al. 2014). On

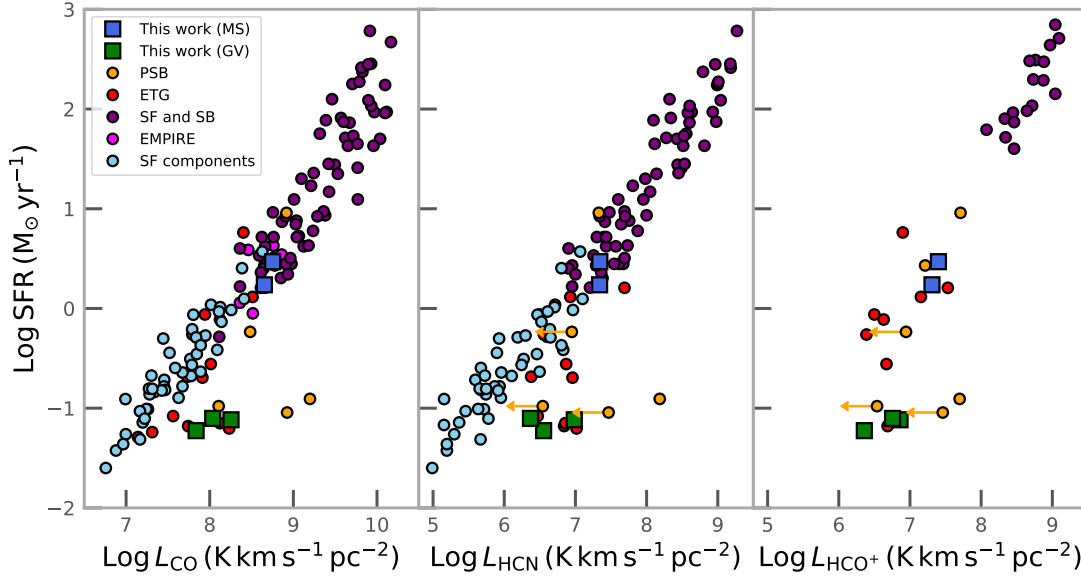


Figure 12. The (global) SFR versus L_{gas} relation for ALMaQUEST galaxies used in this work (main-sequence: blue squares; green valley: green squares), post-starburst galaxies (French et al. 2023), EMPIRE star-forming galaxies (Jiménez-Donaire et al. 2019), ETGs (Crocker et al. 2012), star-forming and starburst galaxies (Gao & Solomon 2004), and subcomponents of star-forming galaxies (Usero et al. 2015). From left to right: CO, HCN, and HCO^+ .

the other hand, our results are consistent with earlier observational studies on kiloparsec (kpc) scales, which have also shown that the dense gas star formation efficiency ($\text{SFE}_{\text{dense}}$) varies with galactic environments and galactocentric radii (e.g., Jiménez-Donaire et al. 2019; Neumann et al. 2023). Therefore, our findings align better with turbulence-regulated models than with fixed-density models (Chen et al. 2015; Usero et al. 2015; Bigiel et al. 2016; Gallagher et al. 2018; Querejeta et al. 2019; Jiménez-Donaire et al. 2019).

One of the keys to study the role of turbulence in shaping SFE is through the study of the velocity dispersion (σ) of the molecular gas at scales close to the molecular clouds. Previous high-resolution observations ($\sim 100\text{pc}$) revealed an strong anti-correlation between $\text{SFE}_{\text{dense}}$ and σ (e.g. Usero et al. 2015; Leroy et al. 2017; Querejeta et al. 2019) as model predictions (Meidt et al. 2020) while some others found the dependence of $\text{SFE}_{\text{dense}}$ on σ is only moderate (Sánchez-García et al. 2022). Owing to the coarse spatial resolution and moderate S/N of the dense gas observations used in this work, it is not feasible to directly examine the link between SFE and velocity dispersion. Future higher resolution data with better sensitivity will further shade light on the physical conditions setting $\text{SFE}_{\text{dense}}$ in green valley galaxies.

4.2. Comparison with previous studies in the literature

After examining the resolved dense gas properties in our sample, we now compare the global dense gas properties of the 5 ALMaQUEST sources with other galaxy populations

to better understand the role of dense gas in the broader context. Figure 12 show the global SFR versus global molecular gas luminosity (L) for the 5 ALMaQUEST galaxies and various samples from the literature, including EMPIRE galaxies (Jiménez-Donaire et al. 2019), post-starburst galaxies (Rowlands et al. 2015; French et al. 2018, 2023), early-type galaxies (Crocker et al. 2012), star-forming and starbursting galaxies (Gao & Solomon 2004), and subregions in star-forming galaxies (Usero et al. 2015). Most of the star-forming populations, including the star-forming galaxies and starbursting galaxies, follow a linear relation for all gas tracers (CO, HCN, and HCO^+) spanning over three orders of magnitude. In contrast, the post-starburst galaxies and ETGs show diverse behaviors, with some on the same trend formed by star-forming galaxies while some others offset from the main relationship toward lower SFE_{mol} as well as lower $\text{SFE}_{\text{dense}}$. The 3 ALMaQUEST green valley galaxies are all below the star-forming linear relationship, similar to those post-starburst galaxies and ETGs that show low SFE_{mol} and $\text{SFE}_{\text{dense}}$. These measurements suggest that there is quite a diversity in these transitioning and/or quenched galaxies (including green valley, post-starburst, and early-type galaxies) in terms of their SFE. Some may have normal SFE as typical star-forming or even starburst galaxies whereas some others have relatively low (dense gas) SFE.

In figure 13, we plot the global SFR versus the ratio of dense molecular gas to total molecular gas traced by $L_{\text{HCN}}/L_{\text{CO}}$ (left panel) and $L_{\text{HCO}^+}/L_{\text{CO}}$ (right panel) for vari-

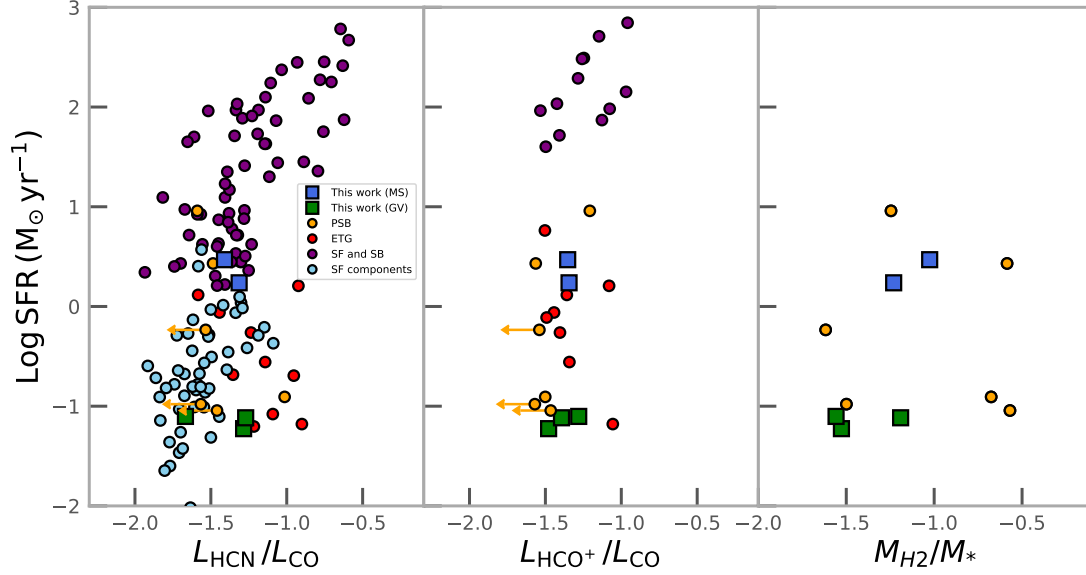


Figure 13. The (global) SFR as a function of dense gas luminosity ratio using $L_{\text{HCN}}/L_{\text{CO}}$ (left panel), $L_{\text{HCO}^+}/L_{\text{CO}}$ (middle panel), and H₂-to-stellar mass ratio (right panel) for ALMaQUEST galaxies used in this work (main-sequence: blue squares; green valley: green squares), post-starburst (PSB) galaxies (French et al. 2023), ETGs (Crocker et al. 2012), star-forming and starburst galaxies (Gao & Solomon 2004), and subcomponents of star-forming galaxies (Usero et al. 2015).

ous types of galaxies. Here we use the line luminosity ratio instead of the gas mass ratio as the dense gas fraction indicator in order to compare different samples in the literature in a more straightforward way. First thing to notice is that at a given population, there is a wide spread in both the $L_{\text{HCN}}/L_{\text{CO}}$ and $L_{\text{HCO}^+}/L_{\text{CO}}$ ratios. There seems to be no strong systematic difference in the ratio of dense molecular gas to total molecular gas with respect to the level of SFR, except that the starburst sample with the highest SFR does extend to the high end of the dense gas fraction. This implies that the dense gas fraction may not play a dominant role in separating the transitioning or quiescent galaxies from the star-forming population. Among the non-star-forming categories, our green valley sample has comparable dense gas luminosity ratio as ETGs and at least half of the post-starburst galaxies that are detected in dense gas tracers. On the other hand, the post-starbursts show a wider distribution in the gas-to-stellar mass ratio compared to the green valley galaxies targeted in this work as revealed in the right panel of Figure 13. The 3 PSBs with highest gas-to-stellar ratio are not necessarily the ones associated with the highest dense gas fractions. There is clear diversity in the gas content of the post-starburst galaxies. In the future, it will be insightful to look into the connection between the dense gas fraction and the star formation histories with a larger sample to understand better whether there is evolution of the dense gas state along different star formation phases.

5. SUMMARY

In this work, we present ALMA HCN(1-0) and HCO⁺(1-0) observations for 5 galaxies selected from the ALMaQUEST survey, including 3 green valley (GV) galaxies and 2 main-sequence (MS) galaxies. These galaxies are previously selected to exhibit comparable molecular gas fractions (f_{mol}) traced by their CO abundance but differences in their molecular gas star formation efficiency (SFE_{mol}), resulting in the difference in the specific star formation rate (sSFR). The aim of this paper is to investigate if the variation in SFE_{mol} between MS and GV galaxies is driven by the lack of dense molecular gas, despite the normal molecular gas abundance, or is due to the low efficiency of forming stars with respect to the dense gas abundance, characterized by $\text{SFE}_{\text{dense}}$. Our main findings can be summarized as below:

1. Both HCN and HCO⁺ are detected in all the five galaxies. The global HCN-to-CO and HCO⁺-to-CO line ratios are found to be 0.02-0.05 and 0.03-0.05, respectively, broadly consistent with the values found in the literature.

2. The dense gas Schmidt-Kennicutt relation is found to be different between MS and GV galaxies, with the latter showing lower Σ_{SFR} for a given Σ_{dense} and hence lower $\text{SFE}_{\text{dense}}$ (Figure 4 and Figure 5). When separating the star-forming and non-star-forming spaxels, it is seen that the non-star-forming spaxels, which dominate the regions of GV galaxies, deviate significantly from the dense gas SK relation

formed by the star-forming spaxels toward lower values of Σ_{SFR} at a given dense gas surface density.

3. The molecular gas based SFE_{mol} (traced by CO) better correlates with $\text{SFE}_{\text{dense}}$ (traced by HCN or HCO^+) than with the dense gas fraction, i.e., dense-to-molecular gas mass ratio (f_{dense}) (Figure 6 and Figure 7). In fact, the ranges of the f_{dense} ratio between star-forming and non-star-forming spaxels, or between MS and GV spaxels, are similar. In other words, SFE_{mol} is primarily set by the ability of dense gas to form stars in our sample.

4. When looking at the dependence of sSFR on various parameters, we find that sSFR is best correlated with the SFE_{mol} and $\text{SFE}_{\text{dense}}$ (with correlation coefficients ~ 0.8 - 0.9), followed by the dependence on the molecular gas fraction (f_{mol}), and is least associated with f_{dense} or the dense-to-stellar mass ratio (Figures 8, 9, and 10). The correlation between sSFR and SFE extends to non-star-forming spaxels as well. Our results suggest that the quenching mechanisms responsible for lowering the star formation activities in these galaxies mainly impact f_{gas} and $\text{SFE}_{\text{dense}}$, and do not alter the dense gas-to-molecular gas ratio directly.

5. The ALMaQUEST green valley (GV) galaxies exhibit systematically lower global SFE_{mol} and $\text{SFE}_{\text{dense}}$ when compared to star-forming and starburst galaxies in previous studies (Figure 12). However, there is no significant distinction between GV galaxies and other types of galaxies in terms of the dense gas luminosity ratio (Figure 13). This aligns with the spatially resolved findings that the low sSFR of our GV galaxies is not attributed to a lack of dense gas.

In conclusion, we find that the 3 GV galaxies in our sample, while having comparable molecular gas fraction (f_{gas}), their spaxel-based f_{dense} are also comparable to that in MS galaxies whereas the SFE_{mol} and $\text{SFE}_{\text{dense}}$ are systematically lower than those of MS galaxies. In other words, these GV galaxies are less efficient in converting dense gas to stars and therefore lead to lower specific star formation rates as opposed to MS galaxies. Nevertheless, We emphasize that the 3 GV galaxies in our sample are CO-abundant by selection and may not be representative of the whole GV population in general. Having a larger GV sample covering a different parameter space may shed light on the connection between star formation and molecular gas, as well as on the physical processes that suppress star formation in GV galaxies.

ACKNOWLEDGMENTS

We thank the anonymous referee for his/her helpful comments, which improve the contents of this paper. This work is supported by the Ministry of Science & Technology of Taiwan under the grants MOST 111-2112-M-001-044 - and NSTC 112-2112-M-001-062 -. HAP acknowledges support by the National Science and Technology Council of Taiwan under grant 110-2112-M-032-020-MY3. N.H. acknowledges support from JSPS KAKENHI grant No. JP21K03634. S.F.S. thanks the support by the PAPIIT-DGAPA AG100622 and CONACYT CF19-39578 projects.

The authors would like to thank the staff of the East-Asia and North-America ALMA ARCs for their support and continuous efforts in helping produce high-quality data products. This paper makes use of the following ALMA data:

ADS/JAO.ALMA#2015.1.01225.S,
 ADS/JAO.ALMA#2017.1.01093.S,
 ADS/JAO.ALMA#2018.1.00541.S,
 ADS/JAO.ALMA#2018.1.00558.S,
 ADS/JAO.ALMA#2019.1.01178.S.

ALMA is a partnership of ESO (representing its member states), NSF (USA) and NINS (Japan), together with NRC (Canada), MOST and ASIAA (Taiwan), and KASI (Republic of Korea), in cooperation with the Republic of Chile. The Joint ALMA Observatory is operated by ESO, AUI/NRAO and NAOJ.

Funding for the Sloan Digital Sky Survey IV has been provided by the Alfred P. Sloan Foundation, the U.S. Department of Energy Office of Science, and the Participating Institutions. SDSS-IV acknowledges support and resources from the Center for High-Performance Computing at the University of Utah. The SDSS web site is www.sdss.org. SDSS-IV is managed by the Astrophysical Research Consortium for the Participating Institutions of the SDSS Collaboration including the Brazilian Participation Group, the Carnegie Institution for Science, Carnegie Mellon University, the Chilean Participation Group, the French Participation Group, Harvard-Smithsonian Center for Astrophysics, Instituto de Astrofísica de Canarias, The Johns Hopkins University, Kavli Institute for the Physics and Mathematics of the Universe (IPMU) / University of Tokyo, Lawrence Berkeley National Laboratory, Leibniz Institut für Astrophysik Potsdam (AIP), Max-Planck-Institut für Astronomie (MPIA Heidelberg), Max-Planck-Institut für Astrophysik (MPA Garching), Max-Planck-Institut für Extraterrestrische Physik (MPE), National Astronomical Observatory of China, New Mexico State University, New York University, University of Notre Dame, Observatório Nacional / MCTI, The Ohio State University, Pennsylvania State University, Shanghai Astronomical Observatory, United Kingdom Participation Group, Universidad Nacional Autónoma de México,

University of Arizona, University of Colorado Boulder, University of Oxford, University of Portsmouth, University of Utah, University of Virginia, University of Washington, Uni-

versity of Wisconsin, Vanderbilt University, and Yale University.

REFERENCES

- Accurso, G., Saintonge, A., Catinella, B., et al. 2017, *MNRAS*, 470, 4750.
- Albaret, F. D., Allende Prieto, C., Almeida, A., et al. 2017, *ApJS*, 233, 25
- Aguado, D. S., Ahumada, R., Almeida, A., et al. 2019, *ApJS*, 240, 23
- Baldwin, J. A., Phillips, M. M., & Terlevich, R. 1981, *PASP*, 93, 5
- Baker, W. M., Maiolino, R., Bluck, A. F. L., et al. 2022, *MNRAS*, 510, 3622
- Baker, W. M., Maiolino, R., Belfiore, F., et al. 2023, *MNRAS*, 518, 4767
- Barrera-Ballesteros, J. K., Utomo, D., Bolatto, A. D., et al. 2020, *MNRAS*, 492, 2651
- Barrera-Ballesteros, J. K., Heckman, T., Sánchez, S. F., et al. 2021, *ApJ*, 909, 131
- Belfiore, F., Maiolino, R., Maraston, C., et al. 2017, *MNRAS*, 466, 2570
- Belfiore, F., Maiolino, R., Bundy, K., et al. 2018, *MNRAS*, 477, 3014
- al.(2003)ber03 Bergvall, N., Laurikainen, E., & Aalto, S. 2003, *A&A*, 405, 31
- Bigiel, F., Leroy, A., Walter, F., et al. 2008, *AJ*, 136, 2846
- Bigiel, F., Leroy, A. K., Jiménez-Donaire, M. J., et al. 2016, *ApJL*, 822, L26.
- Bolatto, A. D., Wolfire, M., & Leroy, A. K. 2013, *ARA&A*, 51, 207
- Bolatto, A. D., Wong, T., Utomo, D., et al. 2017, *ApJ*, 846, 159
- Brownson, S., Belfiore, F., Maiolino, R., et al. 2020, *MNRAS*, 498, L66.
- Bundy, K., Bershady, M. A., Law, D. R., et al. 2015, *ApJ*, 798, 7
- Cano-Díaz, M., Sánchez, S. F., Zibetti, S., et al. 2016, *ApJL*, 821, L26
- Cano-Díaz, M., Ávila-Reese, V., Sánchez, S. F., et al. 2019, *MNRAS*, 489, 1830
- Cardelli, J. A., Clayton, G. C., & Mathis, J. S. 1989, *ApJ*, 345, 245
- Chen, H., Gao, Y., Braine, J., et al. 2015, *ApJ*, 810, 140
- Chiang, I.-D., Sandstrom, K. M., Chasteney, J., et al. 2021, *ApJ*, 907, 29.
- Cid Fernandes, R., Stasińska, G., Schlickmann, M. S., et al. 2010, *MNRAS*, 403, 1036
- Cid Fernandes, R., Stasińska, G., Mateus, A., & Vale Asari, N. 2011, *MNRAS*, 413, 1687
- Colombo, D., Kalinova, V., Utomo, D., et al. 2018, *MNRAS*, 475, 1791
- Crocker, A., Krips, M., Bureau, M., et al. 2012, *MNRAS*, 421, 1298
- Dey, B., Rosolowsky, E., Cao, Y., et al. 2019, *MNRAS*, 488, 1926
- Dou, J., Peng, Y., Renzini, A., et al. 2021, *ApJ*, 907, 114
- Ellison, S. L., Sánchez, S. F., Ibarra-Medel, H., et al. 2018, *MNRAS*, 474, 2039
- Ellison, S. L., Thorp, M. D., Pan, H.-A., et al. 2020a, *MNRAS*, 492, 6027
- Ellison, S. L., Thorp, M. D., Lin, L., et al. 2020b, *MNRAS*, 493, L39
- Ellison, S. L., Lin, L., Thorp, M. D., et al. 2021a, *MNRAS*, 501, 4777
- Ellison, S. L., Lin, L., Thorp, M. D., et al. 2021b, *MNRAS*, 502, L6.
- Ellison, S. L., Wong, T., Sánchez, S. F., et al. 2021c, *MNRAS*, 505, L46
- Enia, A., Rodighiero, G., Morselli, L., et al. 2020, *MNRAS*, 493, 4107.
- Evans, N. J., Heiderman, A., & Vutisalchavakul, N. 2014, *ApJ*, 782, 114.
- Evans, N. J., Kim, K.-T., Wu, J., et al. 2020, *ApJ*, 894, 103.
- Evans, N. J., Kim, K.-T., Wu, J., et al. 2020, *ApJ*, 894, 103.
- Fabian, A. C. 2012, *ARA&A*, 50, 455
- Federrath, C. & Klessen, R. S. 2012, *ApJ*, 761, 156.
- Feldmann, R., Gnedin, N. Y., & Kravtsov, A. V. 2012, *ApJ*, 747, 124.
- French, K. D., Zabludoff, A. I., Yoon, I., et al. 2018, *ApJ*, 861, 123
- French, K. D., Smercina, A., Rowlands, K., et al. 2023, *ApJ*, 942, 25
- Gallagher, M. J., Leroy, A. K., Bigiel, F., et al. 2018, *ApJ*, 858, 90
- Gao, Y., & Solomon, P. M. 2004, *ApJ*, 606, 271
- García-Burillo, S., Usero, A., Alonso-Herrero, A., et al. 2012, *A&A*, 539, A8.
- Goldsmith, P. F. & Kauffmann, J. 2017, *ApJ*, 841, 25.
- Harada, N., Nishimura, Y., Watanabe, Y., et al. 2019, *ApJ*, 871, 238
- Hsieh, B. C., Lin, L., Lin, J. H., et al. 2017, *ApJL*, 851, L24
- Jiang, X.-J., Greve, T. R., Gao, Y., et al. 2020, *MNRAS*, 494, 1276.
- Jiménez-Donaire, M. J., Bigiel, F., Leroy, A. K., et al. 2019, *ApJ*, 880, 127
- Jiménez-Donaire, M. J., Brown, T., Wilson, C. D., et al. 2023
- Kauffmann, G., Heckman, T. M., Tremonti, C., et al. 2003,
- Kennicutt, R. C., Jr. 1998, *ApJ*, 498, 541
- Kennicutt, R. C. & De Los Reyes, M. A. C. 2021, *ApJ*, 908, 61
- Kewley, L. J., Dopita, M. A., Sutherland, R. S., Heisler, C. A., & Trevena, J. 2001, *ApJ*, 556, 121

- Kewley, L. J., Groves, B., Kauffmann, G., & Heckman, T. 2006, *MNRAS*, 372, 961
- Kewley, L. J. & Ellison, S. L. 2008, *ApJ*, 681, 1183
- Lada, C. J., Lombardi, M., & Alves, J. F. 2010, *ApJ*, 724, 687.
- Lada, C. J., Forbrich, J., Lombardi, M., et al. 2012, *ApJ*, 745, 190.
- Law, D. R., Yan, R., Bershady, M. A., et al. 2015, *AJ*, 150, 19
- Law, D. R., Cherinka, B., Yan, R., et al. 2016, *AJ*, 152, 83
- Leroy, A. K., Walter, F., Brinks, E., et al. 2008, *AJ*, 136, 2782
- Leroy, A. K., Walter, F., Sandstrom, K., et al. 2013, *AJ*, 146, 19
- Leroy, A. K., Schinnerer, E., Hughes, A., et al. 2017, *ApJ*, 846, 71
- Lin, L., Belfiore, F., Pan, H.-A., et al. 2017, *ApJ*, 851, 18
- Lin, L., Bau-Ching Hsieh, Pan, H.-A., et al. 2019a, *ApJ*, 872, 50
- Lin, L., Pan, H.-A., Ellison, S. L., et al. 2019b, *ApJL*, 884, L33
- Lin, L., Ellison, S. L., Pan, H.-A., et al. 2020, *ApJ*, 903, 145.
- Lin, L., Ellison, S. L., Pan, H.-A., et al. 2022, *ApJ*, 926, 175
- Longmore, S. N., Bally, J., Testi, L., et al. 2013, *MNRAS*, 429, 987
- Martig, M., Bournaud, F., Teyssier, R., & Dekel, A. 2009, *ApJ*, 707, 250
- McMullin, J. P., Waters, B., Schiebel, D., Young, W., & Golap, K. 2007, *Astronomical Data Analysis Software and Systems XVI*, 376, 127
- Medling, A. M., Cortese, L., Croom, S. M., et al. 2018, *MNRAS*, 475, 5194
- Meidt, S. E., Glover, S. C. O., Kruijssen, J. M. D., et al. 2020, *ApJ*, 892, 73.
- Meijerink, R., Spaans, M., & Israel, F. P. 2007, *A&A*, 461, 793.
- Neumann, L., Gallagher, M. J., Bigiel, F., et al. 2023, *MNRAS*.
- Morganti, R. 2017, *Frontiers in Astronomy and Space Sciences*, 4, 42
- Morselli, L., Rodighiero, G., Enia, A., et al. 2020, *MNRAS*, 496, 4606
- Pan, H.-A., Lin, L., Hsieh, B.-C., et al. 2018, *ApJ*, 854, 159
- Peng, C. Y., Ho, L. C., Impey, C. D., & Rix, H. W. 2002, *AJ*, 124, 266
- Peng, C. Y., Ho, L. C., Impey, C. D., & Rix, H.-W. 2010, *AJ*, 139, 2097
- Pessa, I., Schinnerer, E., Belfiore, F., et al. 2021, *A&A*, 650, A134
- Pessa, I., Schinnerer, E., Leroy, A. K., et al. 2022, *A&A*, 663, A61
- Papadopoulos, P. P., Zhang, Z.-Y., Xilouris, E. M., et al. 2014, *ApJ*, 788, 153.
- Pettini, M., & Pagel, B. E. J. 2004, *MNRAS*, 348, L59
- Querejeta, M., Schinnerer, E., Schrubba, A., et al. 2019, *A&A*, 625, A19.
- Rowlands, K., Wild, V., Nesvadba, N., et al. 2015, *MNRAS*, 448, 258
- Saintonge, A., Catinella, B., Cortese, L., et al. 2016, *MNRAS*, 462, 1749
- Saintonge, A., Catinella, B., Tacconi, L. J., et al. 2017, *ApJS*, 233, 22
- Salim, S., Lee, J. C., Ly, C., et al. 2014, *ApJ*, 797, 126
- Sánchez, S. F., Rosales-Ortega, F. F., Jungwiert, B., et al. 2013, *A&A*, 554, A58
- Sánchez, S. F., Rosales-Ortega, F. F., Iglesias-Páramo, J., et al. 2014, *A&A*, 563, A49
- Sánchez, S. F., Pérez, E., Sánchez-Blázquez, P., et al. 2016, *RMxAA*, 52, 21
- Sánchez, S. F., Pérez, E., Sánchez-Blázquez, P., et al. 2016b, *RMxAA*, 52, 171
- Sánchez, S. F., Avila-Reese, V., Hernandez-Toledo, H., et al. 2018, *RMxAA*, 54, 217
- Sánchez, S. F. 2020, *ARA&A*, 58, 99
- Sánchez, S. F., Barrera-Ballesteros, J. K., Colombo, D., et al. 2021, *MNRAS*, 503, 1615
- Sargent, M. T., Daddi, E., Béthermin, M., et al. 2014, *ApJ*, 793, 19
- Sánchez-García, M., García-Burillo, S., Pereira-Santaella, M., et al. 2022, *A&A*, 660, A83.
- Sarzi, M., Shields, J. C., Schawinski, K., et al. 2010, *MNRAS*, 402, 2187
- Schmidt, M. 1959, *ApJ*, 129, 243
- Schruba, A., Leroy, A. K., Walter, F., et al. 2011, *AJ*, 142, 37
- Shirley, Y. L. 2015, *PASP*, 127, 299
- Singh, R., van de Ven, G., Jahnke, K., et al. 2013, *A&A*, 558, A43
- Smirnova-Pinchukova, I., Husemann, B., Davis, T. A., et al. 2022, *A&A*, 659, A125
- Stasińska, G., Vale Asari, N., Cid Fernandes, R., et al. 2008, *MNRAS*, 391, L29
- Sun, J., Leroy, A. K., Schinnerer, E., et al. 2020, *ApJL*, 901, L8
- Tan, Q.-H., Gao, Y., Zhang, Z.-Y., et al. 2018, *ApJ*, 860, 165.
- Teng, Y.-H., Sandstrom, K. M., Sun, J., et al. 2023, *ApJ*, 950, 119
- Topal, S., Bureau, M., Davis, T. A., et al. 2016, *MNRAS*, 463, 4121.
- Usero, A., Leroy, A. K., Walter, F., et al. 2015, *AJ*, 150, 115
- Utomo, D., Sun, J., Leroy, A. K., et al. 2018, *ApJL*, 861, L18.
- Vulcani, B., Poggianti, B. M., Moretti, A., et al. 2019, *MNRAS*, 488, 1597
- Wake, D. A., Bundy, K., Diamond-Stanic, A. M., et al. 2017, *AJ*, 154, 86
- Wang, E., Lilly, S. J., Pezzulli, G., et al. 2019, *ApJ*, 877, 132
- Wolfire, M. G., Hollenbach, D., & McKee, C. F. 2010, *ApJ*, 716, 1191.
- Wong, T., & Blitz, L. 2002, *ApJ*, 569, 157
- Wu, J., Evans, N. J., Gao, Y., et al. 2005, *ApJL*, 635, L173
- Wuyts, S., Förster Schreiber, N. M., Nelson, E. J., et al. 2013, *ApJ*, 779, 135
- Yan, R., & Blanton, M. R. 2012, *ApJ*, 747, 61